Catalytic Cycle of Type II 4'-Phosphopantetheinyl Transferases

Sabine Gavalda, Alexandre Faille, Simone Fioccola, Minh Chau Nguyen, Coralie Carivenc, Karine Rottier, Yann Rufin, Stéphane Saitta, Georges Czaplicki, Christophe Guilhot, et al.

The catalytic cycle of type II 4´-phosphopantetheinyl transferases

Journal:	*ACS Catalysis*
Manuscript ID	cs-2023-062499.R2
Manuscript Type:	Article
Date Submitted by the Author:	n/a
Complete List of Authors:	Gavalda, Sabine; Institut de Pharmacologie et de Biologie Structurale Faille, Alexandre; Institut de Pharmacologie et de Biologie Structurale Fioccola, Simone; LAAS-CNRS Nguyen, Minh Chau; IPBS Carivenc, Coralie; IPBS Rottier, Karine; IPBS Rufin, Yann; IPBS Saitta, Stephane; IPBS Czaplicki, Georges; IPBS Guilhot , Christophe ; Institut de Pharmacologie et de Biologie Structurale, Chalut, Christian; Institut de pharmacologie et biologie structurale Brut , Marie; LAAS-CNRS Mourey, Lionel; IPBS, Pedelacq, Jean-Denis; Institut de Pharmacologie et de Biologie Structurale,

The catalytic cycle of type II 4′-phosphopantetheinyl transferases

Sabine Gavalda[1,3,], Alexandre Faille[1,4,*], Simone Fioccola[2,*], Minh Chau Nguyen[1,5], Coralie Carivenc[1,6], Karine Rottier[1], Yann Rufin[1], Stéphane Saitta[1], Georges Czaplicki[1], Christophe Guilhot[1], Christian Chalut[1], Marie Brut[2,#], Lionel Mourey[1,#] & Jean-Denis Pedelacq[1,#,$]*

[1]Institut de Pharmacologie et de Biologie Structurale (IPBS), Université de Toulouse, CNRS, Université Toulouse III - Paul Sabatier (UT3), Toulouse, France

[2]LAAS-CNRS, Université de Toulouse, CNRS, UPS, Toulouse, France

[3]Carbios, Parc Cataroux – Bâtiment B80, 8 rue de la Grolière, 63100 Clermont-Ferrand, France

[4]Cambridge Institute for Medical Research, Cambridge Biomedical Campus Keith Peters Building, Hills Rd, Cambridge CB2 0XY, United Kingdom

[5]Department of Pharmacology, University of Colorado School of Medicine, Aurora, CO 80045, USA

[6]Centre de Biologie Structurale, Université de Montpellier, CNRS, Inserm, Montpellier, France

[$]Lead contact

KEYWORDS

PPTase, PptT, *Mycobacterium tuberculosis*, Ppant transfer, X-ray crystallography, molecular dynamics, DFT, QM/MM

ABSTRACT

Polyketides are a diverse class of compounds with significant interest in the pharmaceutical industry. They are synthesized by polyketide synthases (PKS), which consist of large multienzyme systems. Post-translational modification of acyl-carrier protein (ACP) domains is crucial for PKS and fatty acid synthases (FAS) function and involves phosphopantetheinyl transferases (PPTases) that attach a 4'-phosphopantetheine (Ppant) moiety from Coenzyme A (CoA) to a conserved serine residue on the ACP domain. This modification enables communication between the ACP and other enzymatic domains within the same PKS. In *Mycobacterium tuberculosis*, PptT is essential for the bacillus replication and survival during infection. This study focuses on unraveling the activation mechanism of an ACP domain by PptT. It combines biochemical and structural analyses with advanced molecular dynamics simulations to elucidate the precise mechanism of CoA's Ppant arm transfer onto the ACP domain. The findings from this research contribute to a deeper understanding of PKS biosynthesis with major implications for anti-TB drug discovery efforts.

INTRODUCTION

Polyketides represent a chemically and functionally diverse class of compounds that are of great interest in the pharmaceutical industry[1]. Typically, aromatic polyketides are biosynthesized by type II polyketide synthases (PKSs) in an iterative process that involves a small set of discrete proteins. In contrast, the biosynthesis of reduced polyketides, such as the lipids present in the cell envelope of mycobacteria, involves protein domains housed within gigantic multienzyme systems referred to as type I PKSs. Essential for PKS activity are the ketosynthase (KS), acyl transferase (AT), and acyl carrier protein (ACP) domains. AT, often referred to as the “gatekeeper”, catalyzes the transfer of an elongation unit (from malonyl-CoA, (2S)-methylmalonyl-CoA, or carboxyl-acyl-CoA) to the ACP domain, while KS catalyzes the formation of C-C bonds between the acyl-ACP and an elongation unit, resulting in the production of an ACP bound β-keto ester.

Post-translational modification of ACP domains is a universal process indispensable to the proper functioning of PKS molecular factories. This modification is catalyzed by phosphopantetheinyl transferases (PPTases), which utilize coenzyme A (CoA) and divalent cations as cofactors (**Figure 1A**). This step implies the covalent linkage of a 4'-phosphopantetheine (Ppant) moiety from CoA to a conserved serine residue of the ACP domain[2]. Anchoring the starting unit at the SH extremity of the Ppant arm acts as a signal for the "shuttle" ACP domain to communicate with the other enzymatic domains, facilitating the proper reactions. In *Mycobacterium tuberculosis,* PptT is essential for the replication and survival of the bacillus during both acute and chronic phases of infection in mice[3]. Consequently, PptT is the focus of intensive anti-TB drug discovery programs between academia and the pharmaceutical industry[4,5]. In this study, we set out to unravel the intricate steps involved in the activation mechanism of an ACP domain by PptT. Our approach involves a combination of biochemical and structural analyses, as well as cutting-edge density functional theory (DFT)-cluster and quantum mechanics/molecular mechanics (QM/MM) molecular dynamics (MD) simulations, to shed light on the precise mechanism by which the Ppant arm of CoA is transferred onto its cognate ACP domain.

RESULTS

Stability and activity of PptT - Initially, the purification of PptT was carried out in the presence of Mg^{2+} and CoA to ensure its expression in a soluble form[6], without knowledge of whether both cofactors were essential for the enzyme's stability. Considering that Mn^{2+} greatly enhances the activity of Sfp-type PPTases[7] and possibly their stability we implemented a two-step purification procedure in which the immobilized metal affinity chromatography (IMAC) step was performed with 1 mM $MnCl_2$, while the size exclusion chromatography (SEC) step was carried out in the absence of the metal ion. In this scenario, both the extraction and purification buffers lacked CoA. Although the SEC profile and SDS-PAGE confirmed the enzyme's monodispersity and high purity (**Figure S1**), differential Scanning Fluorimetry (DSF) experiments revealed relatively low melting temperature (T_m) values of

approximately 30 ˚C (**Figure 1B**), indicating the low stability of PptT under these conditions. In contrast, when $MnCl_2$ was consistently present throughout the purification process, the T_m values could be increased by approximately 15 ˚C (**Figure 1B**).

Furthermore, we examined the effects of Ca^{2+} and Mg^{2+} on the stability of PptT, as these ions have been reported to facilitate the transfer reaction with homologues of PptT: Sfp from *Bacillus subtilis*[7,8] and PptAb from *Mycobacterium abscessus*[9]. Additionally, we expanded the panel of divalent ions to Ni^{2+} and Co^{2+}. Both ions are commonly used during the IMAC step, and Co^{2+} has shown activity restoration in previous studies[10]. Importantly, these divalent ions were found to be compatible with the PptT conditioning buffer. At a final concentration of 1 mM, each cation affects the stability of the enzyme. Among these cations, Ni^{2+} has the most favorable impact, with T_m values above 55 ˚C, followed by Mn^{2+} and Co^{2+}, while Ca^{2+} and Mg^{2+} exhibits the least advantageous effects, with T_m values as low as 35 ˚C (**Figure 1B**). When divalent ions and CoA are combined, there is a significant increase in the stability of PptT, leading to T_m values up to 10 ˚C higher compared to using the divalent ion alone (**Figure 1B**). In contrast, replacing CoA with the reaction product 3',5'-ADP has a limited effect on the stability of the enzyme, and this effect is observed solely in the presence of Co^{2+} and Ni^{2+} ions.

We also confirmed the enzymatic activity of PptT *in vitro* by using the ACP domain from the type I polyketide synthase PpsC of *M. tuberculosis.* PpsC catalyzes crucial biosynthetic steps in the production of lipid virulence factors, including phthiocerol dimycocerosates and phenolic glycolipids[11]. To facilitate this analysis, we generated a library of fragments centered onto the PpsC ACP domain and selected well-expressed and soluble constructs[12]. The selected ACP fragment (2042-2188) was successfully purified using a two-step purification strategy (see Methods section). Furthermore, we demonstrated that PptT could transfer the P-pant moiety from CoA onto the ACP in the presence of either Mn^{2+} or Mg^{2+}. This transfer was visualized through gel electrophoresis on a 10% polyacrylamide gel containing 2.5 M urea (**Figure 1C**).

Structural changes upon PptT activation – The detailed structural dissection of the catalytic cycle of PptT begins with its three-dimensional structure in the absence of CoA. While previous structural studies

have reported apo forms of Sfp-type PPTases[13,14], purifying PptT in the absence of CoA posed a significant challenge due to its beneficial impact on the stability of the enzyme[6]. From the DSF experiments, we identified Mn^{2+} as a promising cation to successfully compensate for the absence of CoA *in vitro*. Crystals could only be obtained under acidic pH conditions, which can hinder cation binding due to the protonation state of acidic residues involved in coordination, as previously observed by us[9] and others[15]. While the apo-PptT structure confirmed the absence of Mn^{2+} at both sites, we identified one Mg^{2+} ion and its counter acetate ion from the crystallization conditions exclusively at site I. The coordination sphere is completed by the side chain of D114 and four water molecules (**Figure 2A**). Additional density in the active site could be attributed to the vector region containing the thrombin cleavage site (LVPR↓GF) and the NdeI site coding for H-1 and M0 located between the N-terminal 6His tag and the PptT sequence, with the histidine main-chain and side-chain nitrogen atoms at hydrogen bond distances to the oxygen atoms of E157 (**Figure 2A**).

The capture of a CoA molecule in the active site cavity of PptT has minimal impact on the positioning of structural elements within the characteristic α/β fold, despite the large number of polar and apolar interactions involving main-chain and side-chain residues (**Figures 2B and 2D**). Most differences concern the orientation of residue side chains that contribute to the anchoring and stabilization of CoA in the cavity (**Figure 2D**). Notably, the side chain of R48 undergoes a ~120˚ rotation, bringing it in the vicinity of the 3'-phosphate of CoA and forming salt bridges with the amino groups. Mutating this arginine to alanine in PptT slightly decreases the affinity for CoA, with limited effects on the activity[15]. The absence of divalent cations at both sites in the PptT-CoA structure caused by the crystallization conditions at pH 4 as previously observed in the X-ray structure of PptAb[9], disturbs the positioning of side-chain residues involved in metal ion coordination. This is the case for H93, a key player during catalysis[15], where the imidazole ring of H93 undergoes a 125˚ rotation, bringing its δ-nitrogen at hydrogen bond distance to the α-phosphate of CoA (**Figure 2B**). The observed conformational changes in R48, H93, and to a lesser extent R56, between the apo and CoA-bound structures cannot be attributed to the vector tag since they occur at a significant distance from these residues. Interestingly, H-1 and M0 fill the gap left by the absence of the Ppant extremity and the adenosine group, respectively, while the acetate takes the place of the α-phosphate to complete the coordination sphere of Mg^{2+} (**Figure 2D**).

On the other hand, minor conformational changes were observed for residues bordering the Ppant moiety and the tunnel entrance (**Figure 2D**).

Once the Ppant transfer onto an ACP domain is completed, the reaction product 3',5'-ADP is released, and the cycle restarts. Good quality crystals of PptT in complex with 3',5'-ADP were obtained at physiological pH, confirming the presence of Mn^{2+} at both sites with octahedral geometry (**Figure 2C**). The main local rearrangements observed in the complex include the rotation of the side chain of E157 towards site I and the repositioning of the imidazole ring of H93 to favor direct interactions with the 3'-phosphate and the metal ion, while all other side-chain positions remain unchanged (**Figure 2D**).

Overall Structure of PptT-CoA/ACP – In this study, we used a long ACP fragment of PpsC spanning from position 2042 to position 2188, encompassing the N- and C-terminal linker regions. To foster interactions with PptT, we mutated the serine at position 2105 to alanine (S2105A), as previously described[2]. As a result, PptT and ACP lock into an active orientation, with the alanine unable to receive the adjacent Ppant moiety. We determined the X-ray structure of the complex using our previously published three-dimensional structure of the PptAb-ACP complex as a model[9]. Analysis of the crystal packing revealed the presence of two ACP molecules in the asymmetric unit, each sandwiched between two PptT molecules (**Figure 3A**). All four PptT structures exhibit high similarity, with a maximum r.m.s.d. of 0.8 Å after superimposition over all 225 Cα atoms, and no significant difference in the assignment of structural elements. Individual ACP structures also closely superimpose with a r.m.s.d. of 1.4 Å over 85 Cα atoms. Significant conformational changes occur in a stretch of unstructured residues in the N-terminal region, stabilized through numerous van der Waals interactions implying an adjacent PptT molecule (**Figures 3B,C**).

The PptT-ACP complex and its interacting region exhibit similarities to other PPTase-ACP complexes previously described by us[9] and others[13,16]. Two patches of residues in loop regions located on the surface of PptT, previously designated as segments S1 (positions 40 to 51) and S2 (positions 116 to 174)[9], cap the region containing the modified S2105 in the ACP domain, burying an average of 650 $Å^2$ at the interface (**Figures 3B,C and Figure S2**). Notably, Y160 drew our attention for two reasons: (i)

its hydroxyl group can interact with the indole NH of W2129 in the ACP domain of one of the complexes (**Figure 3C**) and (ii) it forms, along with E157, W170, and F173, a conserved cluster of four residues that define the tunnel entrance for the pantothenic acid (PA) group of CoA (**Figure 4**). The coordinated changes in the orientation of the side chains of Y160 and W170 (the indole ring is flipped by 180˚ between the apo-PptT and PptT-CoA structures) significantly impact the widening of the tunnel entrance in the presence of PA, accompanied by a noticeable increase in the distance between their closest atoms when PA is absent from the tunnel (**Figure 4**).

Molecular Dynamics study of PptT-CoA/ACP and CoA conformation - Molecular Dynamics (MD) simulations were used to study the conformational changes of CoA-bound PptT upon interactions with the ACP domain and to prepare the complex structures for subsequent QM/MM calculations. To this end, we have compared the systems in the absence and in the presence of ACP. From the classical MD, both complex structures are very stable along the trajectories, with RMSD fluctuations (calculated on the backbone atoms) around 0.2 Å with and without ACP (**Figure S3**).

Important features identified from structural experiments are all conserved. One can notably cite the triad consisting of residues D114, E116 and E157, which coordinates the Mg^{2+} ion at site I. The orientation of the side chain of R48 and the imidazole ring of H93 toward the 3'-phosphate of CoA remains stable (**Figures 5A and 5B**). However, the main difference is observed around the pyrophosphate group. In the absence of ACP, a significant fluctuation of the Oβ-Pβ-Oα-Pα dihedral angle is observed, with values ranging from ±180 to -60˚ (**Figure S4A**). This motion is characterized by a flip of the Pα-Oα-Pβ bridge, with the oxygen atom oriented toward and outside the active site, as shown in **Figures 5A and 5B**, respectively. One should note that this conformational change does not affect the interaction between the Mg^{2+} ion and the Pβ phosphate group at site I, which remains at a distance of approximately 1.9 Å. In the presence of ACP, a different behavior is observed. Upon releasing restraints on the CoA atoms, during the equilibration process, the CoA pyrophosphate stabilizes in a different state. As depicted in **Figure S4B**, the Oβ-Pβ-Oα-Pα dihedral angle exhibits very small fluctuations around 170˚. While this value is close to the range of 180˚ previously observed without ACP (**Figure 5A**), the conformation is distinct. **Figure 5C** shows that the oxygen atom from the Pα-Oα-Pβ bridge is oriented

toward the active site, while the Pβ phosphate group has rotated. It is replaced by a water molecule that coordinates with the Mg^{2+} ion, also interacting with E157. The acceptor residue S2105 in the ACP domain forms stable hydrogen bonds with both the Pβ phosphate group and the residue E157. Consequently, E157 side chain is displaced by 1 Å, creating space for the insertion of a water molecule and the rotation of the Pβ phosphate group. It is noteworthy that the same result was obtained from different starting CoA conformations (**Figure S5**). This state, previously observed in the work by Nguyen et al.[9] and exemplified in **Figure S6**, is catalytically relevant. Further discussion on this topic is provided in the following section, where we describe the quantum mechanics treatment of the obtained active site arrangement to explore the possible reaction paths leading to Ppant transfer.

QM cluster and QM/MM study of the Ppant transfer reaction – Both density functional theory (DFT)-cluster and quantum mechanics / molecular mechanics (QM/MM) calculations were used to elucidate the possible reaction pathways. From the DFT-cluster approach, we optimized the geometry of the reactant, intermediates and transition states (TSs), facilitating a rapid screening of the reaction mechanism. Beginning with the reactant (**Figure S7A**), we propose a reaction intermediate where the oxygen of residue S2105 is bound to the β-phosphate of CoA, while its proton is transferred to an oxygen of residue E157. The reaction enthalpy was determined to be 10.5 kcal/mol, accompanied by an energy barrier of 40.1 kcal/mol (**Figure S8**). Analysis of the intermediate structure (**Figure S7B**) revealed the notable breakage of the phosphodiester bond Pα-Oα-Pβ, suggesting a bimolecular reaction mechanism. We then modeled the product in which the 3',5'-ADP moiety, dissociated in the intermediate, is protonated by an activated metal-bound water molecule (**Figure S7C**). This subsequent reaction, when compared to the intermediate, was found to be exothermic, with an energy barrier of 4.5 kcal/mol and a reaction energy of 0.4 kcal/mol (**Figure S8**).

To gain a more comprehensive understanding of enzyme reactions and consider the whole environment, we implemented a QM/MM steered molecular dynamics (SMD) protocol, in which the QM region was expanded and treated at the semi-empirical PM6 level of theory[17]. To accelerate the SMD simulations without introducing bias due to large dispersion in the non-equilibrium work

distribution[18–20], we applied the Jarzynski relationship[21] to estimate the free energy (a detailed discussion is presented in the following section). This enabled us to thoroughly examine various reaction pathways implicated in the enzymatic reaction.

We first investigated the dual mechanism proposed by Pedelacq and colleagues[9]. In their model, the first step of reaction involves the deprotonation of the hydroxyl group of the serine acceptor (S2105 in ACP), either by the conserved metal-bound glutamate side chain (E157 in PptT) or alternatively an activated metal-bound water molecule. This step is followed by a nucleophilic attack on the β-phosphate of CoA. Although both reaction models propose the formation of an intermediate alkoxide group on S2105, our SMD trajectories do not support this hypothesis. Indeed, a stable alkoxide ion was not observed in our simulation (**Figures S9 & S10**). As a result, we propose a slightly different reaction model, suggesting that proton transfer and nucleophilic attack occur simultaneously in a concerted manner, as illustrated by the model in steps 1a and 1b (**Figure 6A)**, respectively. For both reaction pathways, we observed the formation of a stable intermediate, labeled as IM1a and IM1b (**Figure 6B**). These intermediates correspond to a PptT-CoA/ACP complex with a Mg^{2+} distorted coordination sphere, as depicted in **Figure 6A**. This observation, in contrast to the results obtained from the quantum cluster model, suggests that the nucleophilic substitution at the phosphorus could take place with a unimolecular SN1 associative mechanism. Additionally, a notable change was observed in the dihedral angle Oγ-Cα-Cβ-N of S2105 shifting from 90˚ to 0˚ along trajectories (**Figure 6A**). Simultaneously, the Pα-Oα-Pβ angle flipped by approximately 180˚ from its initial position **(Figure 6A,** IM1a and IM1b). This rotation is suggested to be the driving force behind the reduction of the serine-pyrophosphate distance during the nucleophilic attack. Based on the calculated energy difference of 8.4 kcal/mol between the transition states (TS) 1a and 1b from the two proposed pathways, we conclude that step 1a, which is associated with the formation of IM1a, is energetically more favorable than step 1b associated with IM1b (**Figure 6B**).

In step 2a (**Figure 6A**), we simulated the subsequent dissociation of the 3',5'-ADP moiety from the PptT-CoA/ACP complex, leading to the formation of a second intermediate, named IM2a. As for the quantum cluster model, we propose an additional step, step 3, in which the Oα atom abstracts a hydrogen atom from an activated metal-bound water molecule (**Figure 6A**). This leads to the formation

of a protonated 3',5'-ADP moiety with lower reactivity compared to the unprotonated form, as indicated by our relaxation calculation in NPT (isothermal-isobaric) ensemble. We named the resulting product P1a (**Figure 6B**) We also explored an alternative pathway, named step 2b, in which protonation and dissociation of 3',5'-ADP from the complex occur in a concerted manner (**Figure 6A**), resulting in the formation of the product named P1b. Comparing the Potential of Mean Force (PMF) extrapolated from SMD, we noted that the energy barrier in the mechanism route step 2b is 4.8 kcal/mol higher than the energy observed for TS2a in step 2a (**Figure 6B**). This difference suggests that the final product is formed through the pathway in which dissociation of the 3',5'-ADP moiety and Oα protonation occur stepwise rather than in a concerted manner. **Table I** summarizes significant interatomic distances observed for the reactant, transition states, intermediates, and product structures. It is crucial to note that the transition state structures presented in the table correspond to configurations extracted from the highest points of the PMF profiles. Furthermore, it is essential to highlight the chemical equivalence of products P1a and P1b, as they result from the dissociation of the 3',5'-ADP moiety from the PptT-CoA/ACP complex and its protonation. SMD simulations indicate that P1b possesses a higher energy (20.9 kcal/mol) compared to P1a (15.2 kcal/mol), as depicted in the reaction pathway illustrated in **Figure 6**. This discrepancy in energy can be attributed to the difference in distance between the protonated ADP moiety and the complex. Specifically, in P1a, the distance between PβCoA and OαCoA is measured at 4.04 Å, whereas it is shorter in P1b, measuring 3.28 Å (**Table I**).

DISCUSSION

4′-Phosphopantetheinyl transferases (PPTases) are receiving increased attention due to their essential role in the biosynthesis of a broad range of natural lipids, including lipopolysaccharides and membrane lipids, in all three domains of life. In this study, we focused on PptT, a critical enzyme for the growth of *Mycobacterium tuberculosis in vitro* and during infection in mice[3]. PptT catalyzes the transfer of a 4′-phosphopantetheinyl moiety of coenzyme A (CoA) to an ACP domain of type-I polyketide synthases and non-ribosomal peptide synthases. Although three-dimensional structures of Sfp-type PPTases, including the mycobacterial PptT and PptAb enzymes (69 % sequence identity), have been described

either alone or in complex with an ACP domain[9,15,16,22], significant unanswered questions remain regarding the chronological events preceding the activation of an ACP domain and the mechanism of Ppant transfer leading to the formation of the reaction product 3',5'-ADP. This study provides a unique opportunity to recapitulate these events by combining a detailed structural analysis of key steps with cutting-edge DFT-cluster and QM/MM MD simulations, offering unparalleled insights into the activation process.

In the apo-PptT structure, the void is filled by a histidine residue (H-1) and the initiator methionine (M0) from an adjacent PptT macromolecule in the crystal packing, replacing the Ppant arm and the adenosine group, respectively (**Figure 2A**). To investigate the potential inhibition of PptT activity *in vitro*, we incubated PptT with a synthesized His-Met dipeptide (data not shown). The rationale behind this experiment was to determine if the dipeptide could bind to PptT and inhibit its activity, thereby serving as a promising inhibitor for future studies. Regrettably, no significant inhibition of PptT activity was observed. Furthermore, our attempts to crystallize the PptT/His-Met complex were unsuccessful, suggesting that the dipeptide may not bind tightly or specifically to the active site of PptT.

We previously demonstrated that divalent metal ions are essential for the post-translational modification reaction of ACP domains. In the active site cavity of PptAb of *M. abscessus*[9], two metal ion binding sites have been identified, which are also present in the PptT structure (**Figure 2C**). Site I plays a crucial role in enzymatic activity by favorably orienting the side chain of the key catalytic residue E157, while site II contributes significantly to the stability of the enzyme through numerous direct and indirect water-mediated interactions. The fact that metal binding can occur independently of CoA binding suggests a two-step scenario in which metal ions bind first, followed by CoA. This process would involve the local repositioning of the metal ions, water molecules, and side-chain residues, ultimately completing the coordination sphere. CoA binding also leads to significant structural rearrangements in two regions of the PPTase. Most of changes occur in residues R48, R56, and H93. The first two residues stabilize the ribose moiety through direct interactions with the 3'-phosphate group, while H93 is involved in stabilizing the 3'-phosphate and α-phosphate of the 3',5'-ADP moiety.

Despite the increasing number of isolated type I ACP structures in the PDB, there is limited information available regarding the structural organization of the linker regions at the N- and C-terminal

extremities. Using the AlphaFold2 server (https://colab.research.google.com/github/sokrypton/ColabFold/blob/main/AlphaFold2.ipynb), we conducted a 3D structure prediction for the ACP domain of PpsC, as depicted in **Figure S11A**. This prediction unveiled a 16-amino acid-long random coil starting at position 2041, as well as a 21-amino acid-long unstructured segment followed by a 20-amino acid-long α-helical segment that initiates at position 2145. This α-helical segment, also referred to as the docking domain (DD)[23], plays a crucial role in mediating protein-protein interactions between the upstream ACP and the downstream DD of the ketosynthase (KS) domain within PpsD, thereby facilitating the transfer of the polyketide chain. In our previously reported X-ray structure of the PptAb-ACP complex[9], only the amino acid residues constituting the protein core of the ACP domain were visible in the electron density map (**Figure S11B**). In this study, approximately half of the N-terminal region could be reconstructed, attributed to stabilization effects with an adjacent PptT molecule within the crystal lattice. However, the predicted α-helical region in this segment could not be confirmed (**Figure S11C**). In contrast, residues within the C-terminal region remain indiscernible.

In a previous study, we identified two potential activation pathways in the initial step of the Ppant arm transfer mechanism on the ACP domain[9]. One pathway involves the metal-bound E157, abstracting the hydrogen from S2105, while the other suggests deprotonation of the hydroxyl group of S2105 by an activated metal-bound water molecule. To investigate these pathways, we conducted molecular modeling coupled with QM/MM calculations. Our findings revealed that the absence of an intermediate alkoxide group conflicts with the hypothesis of a concerted proton transfer and a nucleophilic attack on the β-phosphate of CoA. Subsequently, the reaction favors a transition state where E157 abstracts the hydrogen from S2105 in the ACP domain (**Figure 6A**).

Furthermore, we investigated the protonation reaction of the 3',5'-ADP moiety using both the QM/MM and quantum cluster methods. While both methods consistently described this process, the quantum cluster model suggests, in contrast to the QM/MM model, a bimolecular reaction mechanism resulting in the formation of a single intermediate. This discrepancy underscores the limitations of the quantum cluster model in fully capturing the complexity of the enzymatic environment. For instance, the restricted size of the active site excludes specific effects from solvent or distant residues that may be

crucial for catalytic activity. Additionally, allosteric and entropic effects are generally not accounted in this approach.

Analysis of the energy profiles also reveals disparities between models, with the QM/MM method showing a reaction energy of 15.2 kcal/mol (**Figure 6B**), potentially overestimated due to the application of a semiempirical level of theory. In contrast, the DFT cluster model, yielded a more reasonable reaction energy of 0.4 kcal/mol (**Figure S8**). However, the same DFT cluster model shows an overestimated energy barrier of 40.1 kcal/mol for the TS1 transition state compared to 19.0 kcal/mol calculated with the QM/MM approach (TS1a). This difference may be attributed to the inherent simplifications in the cluster model (**see Methods section**) and the stabilizing effect of a more complex environment considered in the QM/MM calculations. Notably, the DFT cluster calculations provide energies for the intermediate (IM) and TS2 states, with values of 10.5 kcal/mol and 15.0 kcal/mol, respectively, falling within the same range as those found with QM/MM. Despite differences in the first energy barrier, both methods yield similar path profiles, with step 1 emerging as the limiting step in both cases. Both methods converge on predicting an endergonic reaction energy and similar geometries, thereby reinforcing our proposed pathway.

The attractiveness of PPTases as targets for the development of new drugs has fueled numerous research initiatives. In the case of Mtb PptT, collaborative efforts between academia and the pharmaceutical industry have led to the identification of promising molecules, such as amidinourea 8918, and subsequent amidino-derived compounds active against PptT both *in vitro* and *in vivo*[4,5] and PptAb *in vitro*[24]. However, further optimization of these molecules is still necessary. A recent high-throughput screening campaign against PptT has emphasized the importance of obtaining an experimentally solved apo structure, as ligand binding can alter the active site, potentially hindering inhibitor discovery[25]. Taking advantage of the structural changes associated with the four major steps of the PptT catalytic cycle described in this study could benefit the chemical structure optimization of new compounds.

METHODS

Cloning of PptT and ACP constructs – The gene encoding wild-type PptT was cloned using NdeI and BamHI restrictions sites under the control of the tet promoter (P_{tet}) from a pTet vector, which contains the spectinomycin resistance marker ($Spec^R$), a ColE1 origin of replication and the gene encoding tetracycline repressor (Tet^R)[6]. The resulting plasmid was introduced into chemically competent *E. coli* BL21(DE3) cells (Invitrogen, Carlsbad, CA, USA) to overproduce PptT fused with a N-terminal 6his tag.

The fragment encoding the ACP domain (positions 2042-2188) was PCR amplified using *ppsC* as a DNA template and gene specific forward 5'-GATATACATATGCATGACTCGGCGGCCCGCAAAA-3' and reverse 5'-GAATTCACTAGTTGACTCGCCTCGCGTCGCAGCTT -3' primers with NdeI and SpeI restriction sites in bold. The digested product was then inserted into a commercially available pET28 vector (Novagen, Madison, WI, USA) with a N-terminal 6His tag. Ligated plasmids were transformed into chemically competent *E. coli* BL21ΔentD[26].

Transformed cells expressing PptT or ACP were plated onto Luria-Bertani (LB) agar plates containing 75 μg/mL spectinomycin or 35 μg/mL kanamycin for overnight growth at 37 ˚C, respectively. The selected clones were grown in 5 mL culture containing the same antibiotics. 10 mL of cell cultures were diluted 50 times in LB including glycerol 20% for a -80 ˚C freezer stock. DNA was sequenced by Eurofins (Konstanz, Germany). The S2105A ACP fragment was created by reassembly PCR, as previously described[9].

Production, purification of PptT and complexes with CoA and 3',5'-ADP – Frozen cells expressing the full-length PptT were used to start an overnight 3 mL LB-spectinomycin culture at 32 ˚C prior to inoculation in baffled flasks containing 500 mL of the same media. Cells were allowed to grow for approximately 2 h at 37 ˚C before temperature was dropped from 37 ˚C to 20 ˚C. When OD_{600} reached 0.5–0.7, cells were induced with 0.3 μg/mL anhydrotetracycline (AnTET) and grown for an additional 18 h prior to harvesting by centrifugation at 4000xg for 30 min and storage at -80 ˚C. Bacterial cell pellets were resuspended in 20 mL buffer A (100 mM Tris pH 7.0, 300 mM NaCl, and 1 mM $MnCl_2$) to

maintain it in its apo form. After sonication (6 cycles of 30 s pulse, 50% amplitude, power 5) and centrifugation at 30,000x*g* for 30 min, the lysate was loaded onto a 1 mL HisTrap HP (GE Healthcare) affinity column pre-equilibrated with the same buffer. Apo-PptT was eluted using a 15 % step of buffer B (100 mM Tris pH 7.0, 300 mM NaCl, 300 mM imidazole, and 1 mM $MnCl_2$). Apo-PptT was then concentrated using a Vivaspin 20 centrifugal concentrator (Sartorius), prior to injection into a size-exclusion column (HiLoad 16/60 Superdex 75, GE Healthcare) pre-equilibrated with buffer C (50 mM Tris pH 7.0, 50 mM NaCl, 1 mM $MnCl_2$). Except for some DSF experiments where $MnCl_2$ was removed during size-exclusion chromatography, the same protocol was applied for the production of PptT-CoA and PptT-3',5'-ADP with cofactors in the resuspension buffers A and B at final concentration of 50 µM and 100 µM, respectively. Removal of the N6His tag was necessary for the crystallization of PptT in complex with ACP and the reaction product 3',5'-ADP. The pooled fractions were mixed with thrombin (1 UE for 2 mg of protein, Novagen) to cleave the 6His tag during dialysis in buffer D (100 mM Tris pH 7.0, 100 mM NaCl, 1 mM $MnCl_2$) at 4 ˚C for 2 h. An additional run through the HisTrap HP column was necessary to eliminate the residual tagged protein. Unbound PptT was then concentrated using a Vivaspin 20 centrifugal concentrator (Sartorius), prior to injection into a size-exclusion column (HiLoad 16/60 Superdex 75, GE Healthcare) pre-equilibrated with buffer C.

Production and purification of the ACP domain – Frozen cells expressing the PpsC ACP fragment were used to start an overnight 5 mL LB culture at 32˚C supplemented with 35 µg/mL kanamycin. This starter culture was used to inoculate one baffled flask with 0.5 L of the same media. Cells were allowed to grow for approximately 2 h at 37 ˚C before temperature was dropped to 30 ˚C. When OD_{600nm} reached 0.5, cells were induced with IPTG at a final concentration of 0.5 mM and grown for an additional 4 h prior to harvesting by centrifugation at 4000x*g* for 30 min and storage at -80 ˚C. The pelleted cells were suspended in 15 mL buffer E (100 mM Tris pH 7.0, 300 mM NaCl) and lysed by sonication (4 cycles of 30 s pulse, 50% amplitude, power 5) prior to centrifugation at 30 000x*g* for 45 min. The supernatant was mixed with 2 mL of cobalt Talon Superflow resin (GE Healthcare 28-9575-02) and left on ice for 10 min. After removal of the supernatant, three cycles of resuspension/centrifugation of the ACP-bound resin were used to ensure thorough washing before the elution of non-specific contaminants in the

presence of buffer E containing 10 mM imidazole. Finally, the 6his-ACP was eluted using the same buffer supplemented with 300 mM imidazole. The eluted protein fractions were pooled, and the 6His tag was removed following the procedure described above. The untagged protein was concentrated using a Vivaspin 20 centrifugal concentrator (Sartorius), prior to injection into a size-exclusion column (HiLoad 16/60 Superdex 75, GE Healthcare) pre-equilibrated with buffer F (50 mM Tris pH 7.0, 50 mM NaCl).

DSF experiments – Fluorescence of the SYPRO Orange Protein Gel Stain (Invitrogen, USA) was measured using the CFX96 real-time PCR detection System (Bio-Rad, Hercules, CA, USA). Fluorescence emission measurements were monitored at 610 nm from 20 ˚C to 90 ˚C in 0.3 ˚C increments. DSF assays were performed in 96-well clear-bottom Hard-Shell Low-Profile 96-Well Plates (BioRad). PptT purified in the presence of 1 mM $MnCl_2$ was injected onto a Superdex 75 analytical column (GE Healthcare) pre-equilibrated with 50 mM Tris pH 7.0, 50 mM NaCl, to remove excess Mn^{2+}. 25 µl assays were conducted with 3 µM PptT, 100 mM Tris buffer (pH 7 or 8), 1 mM divalent cations (Ca^{2+}, Mg^{2+}, Mn^{2+}, Co^{2+}, or Ni^{2+}), 50 µM cofactors (CoA and 3',5'-ADP), and 10x of Sypro Orange. Each condition was carried out in triplicate. Melting temperatures were then calculated using the BioRad CFX Manager software.

Activity assays – Activity assays were conducted in the presence of 50 nM PptT, 10 µM PpsC ACP domain, 50 mM Tris pH 7, 50 µM CoA, 10 mM DTT and 1 mM divalent cations ($CaCl_2$, $MnCl_2$ or $MgCl_2$). The reaction mixture was incubated at 30 ˚C. Aliquots were then removed at different times and the reaction was stopped in the presence of 100 mM EDTA. Samples were then loaded on a 10% polyacrylamide gel supplemented with 2.5 M urea.

X-ray structure determination – Highly purified proteins were crystallized in Innovaplate™ SD-2 Crystallography Plate (Innovadyne Technologies Inc., USA) using commercially available kits from Qiagen (Venlo, Netherlands). Drop sizes of 0.4 µL containing a protein:reservoir ratio of 1:1 were set

up using the Innovadyne™ Nanodrop™ ExtY dispenser (Innovadyne Technologies Inc., USA). Crystals were all flash frozen directly from the crystallization mixture in liquid nitrogen).

Purified PptT-CoA was concentrated to ~400 µM. Diffraction quality PptT-CoA crystals could be obtained within three weeks in the presence of 0.1 M phosphate/citrate pH 4.0, 22% PEG 1000, 0.2 M Li_2SO_4. In order to accelerate PptT crystals growth, we adapted a microseeding protocol where crushed platelets served as microseeds for the setup of new crystallization trials[27,28]. One highly redundant sulfur SAD data set was collected at a wavelength of 2 Å at the ESRF beamline ID29 (Grenoble, France). Crystals belong to space group $C222_1$ with cell parameters a=99.8 Å b=121.3 Å, c=48.8 Å and one molecule per asymmetric unit. A total of 12 anomalous scatterers, 8 sulfur atoms from 4 cysteines and 4 methionines in addition to the 3 phosphorus and the sulfur atoms from CoA, could be identified and the X-ray structure of PptT was solved at 2.1 Å resolution. Phases have been extended to 1.4 Å resolution using an X-ray diffraction dataset collected at the SOLEIL beamline PX1 (Gif-sur-Yvette, France). The final model has been refined at 1.4 Å resolution to an R-factor of 0.14% and an R-free of 0.17% (Table S1).

Single crystals of apo-PptT concentrated to ~400 µM were obtained in 0.1 M Na acetate pH 4.6, 3 M Mg acetate. Diffraction data were collected at a resolution of 1.7 Å on the ESRF ID23-2 beamline. Crystals of the PptT-3',5'-ADP concentrated to ~200 µM in 0.1 M HEPES pH 7.5, 20 %w/v PEG 4K, 10 %v/v 2-Propanol, diffracted to a maximum resolution of 2.5 Å on beamline ID23-1 at the ESRF.

PptT at 350 µM was mixed with the PpsC ACP domain in a 1:0.9 molar ratio, in the presence of 50 µM CoA and 1 mM $MgCl_2$. Plate-like crystals were obtained in the presence of 0.1 M HEPES pH 7.5, 10 % isopropanol, 20 % PEG4000. Optimization of crystallization conditions was realized using our Biomek® FX^P robot (Beckman Coulter, Inc., USA) and manually in Linbro plates (Hampton Research, Aliso Viejo, USA) containing 500 µl reservoir solution. Best crystallization conditions correspond to 0.1 M HEPES pH 7.25, 5 % isopropanol, 24 % PEG4000. Thin platelets were obtained that diffracted to a resolution limit of 2.5 Å at synchrotron sites. A complete X-ray diffraction dataset at 2.5 Å resolution was collected at the beamline XALOC at the ALBA synchrotron in Barcelona, Spain.

X-ray structures of apo-PptT, PptT-CoA/ACP, and PptT-3',5'-ADP were solved by molecular replacement using coordinates of PptT from the PptT-CoA structure as a template in PHASER[29]. Iterative cycles of manual model building in COOT[30] and refinement procedures using PHENIX refine[31] were applied until convergence. Details concerning all data collection and refinement statistics are indicated in **Table S1**.

Molecular Dynamics protocol – All classical MD simulations were carried out using the AMBER package[32] with the FF14SB force field[33]. The parameters of CoA and Mg^{2+} ions were extracted from the AMBER parameter database[34,35] and prepared with Antechamber programs[36]. The LEaP module was used to prepare the systems (PptT-CoA and PptT-CoA/ACP) and the H++[37] server to adjust the residue protonation states at pH 7 (the effect of pH is discussed in **Figure S12**). Both systems were studied in explicit solvent, surrounded with a rectangular water box (with a separation of 10 Å between the protein and the sides of the box), using the TIP3P model[38]. Na^+ counterions were added to neutralize the total charge. For each prepared complex, 50,000 cycles of energy minimization were first performed with a 500 $kcal \cdot mol^{-1} \cdot Å^{-2}$ constraint applied to the solute. A second minimization without restraint was performed on the whole system. Subsequently, the entire system was heated from 0 to 300 K during 200 ps using the Langevin thermostat with a collision frequency of 2 ps^{-1}, at constant volume. The restraints initially applied on the complex were slowly released during the heating process and the system was then equilibrated for another 200 ps. Finally, the production setup was implemented in the NPT ensemble with 1 atm target pressure using the Berendsen barostat with a pressure relaxation time of 2 ps. Long-range electrostatic interactions were treated using the particle-mesh Ewald method with a 12.0 Å cutoff while covalent bonds involving hydrogen atoms were constrained using the SHAKE algorithm with 2 fs integration time step. Analyses were performed with the CPPTRAJ module of AMBER16[39], while the Visual Molecular Dynamics software[40] was used to visualize the trajectories. The resulting trajectories are 50 ns in duration. Clustering was subsequently performed to extract significant structures as starting points for the subsequent QM/MM calculations.

DFT-cluster protocol - The cluster model consists of 126 atoms, including a section of the CoA substrate where the cysteamine tail and adenine base have been truncated and replaced by a hydrogen atom. It also includes Mg^{2+} metal ions and the side chains of H93, D114, E116, E157 and S2105 (**Figure S7A**). However, crucial residues in the vicinity of the catalytic site, such as T92 and K161, which may significantly stabilize the PptT-CoA/ACP complex, as predicted in QM/MM calculations, were not incorporated into the model. Geometrical optimizations were carried out using DFT, threatening the system with the hybrid B3LYP[41,42] functional in conjunction with the Grimme's D3 dispersion[43] correction. The Ahlrichs def2-TZVP[44] basis set was applied to all the atoms, except for metal ions, where the aug-cc-pVDZ[45] was used. Solvation was included using the conductor-like polarizable continuum model (CPCM)[46] method to estimate the surrounding effects of the protein, with a chosen dielectric constant of 4.

QM/MM dynamics protocol - The PptT-CoA/ACP structure, previously obtained from classical MD, was used for QM/MM calculations and SMD. We have considered a 179-atom QM region, with a net charge of -4. This QM region includes two Mg^{2+} ions coordinated by five water molecules, the CoA ligand, and specific residues: E116, E157 and D114 coordinating Mg^{2+} at site I; H93 coordinating Mg^{2+} (II); and D2104 and S2105 from the ACP domain. The QM/MM boundary cuts were applied to C-C bonds, and the edges were treated with hydrogen atom links.

During the QM/MM simulations, the quantum part was treated at the semiempirical PM6 level of theory, while the MM region was evaluated using the classical ff14SB force field[33]. The nonbonded cutoff for the long-range electrostatic interactions was set at 12 Å and 8 Å for the MM and QM regions, respectively. In the first place, the system was minimized without constraint employing the steepest-conjugate gradient scheme. It was then heated in the NVT ensemble for 50 ps at 1 fs/step and equilibrated at a constant density for 25 ps using the same ensemble. The stochastic Langevin thermostat[47] was used to keep the temperature at 300 K with a collision frequency of 2 ps^{-1}. During the heating and equilibration steps, a harmonic restraint was applied on the PptT backbone and ACP domain,

with a force constant of 10 kcal·mol^{-1}·Å^{-2} initially, which was subsequently reduced to 1 kcal·mol^{-1}·Å^{-2}. Finally, the system was equilibrated in the NPT ensemble for 50 ps without any restraints, and the pressure was maintained around 1 atm using the Berendsen barostat[48] with a pressure relaxation of 2 ps. Throughout all steps, the SHAKE algorithm[49] was enabled to constraint bonds involving non-polar hydrogen atoms. From the last equilibration run, we extracted a snapshot corresponding to the shortest interatomic distance found between OγS2105-PβCoA (4.66 Å) and HγS2105-OεE157 (1.81 Å). The extrapolated structure was considered as the initial configuration (the reactant R indicated in the energy graph of **Figure 7B**) for step 1a and 1b. The graphical representation is included in **Figure 6A.**

SMD protocol – In all simulated reaction steps, 96 SMD trajectories were performed in the NPT ensemble equilibrated at 300 K and 1 atm. A light harmonic restraint of 1 kcal·mol^{-1}·Å^{-2} was applied to the backbone of PptT, the two Mg^{2+} ions, and to the ACP domain, except for residues near to S2105 (ranging from positions 2100 to 2108). The SHAKE algorithm was turned off only for the hydrogen bonds involving residues belonging to the QM region that participate in the reaction: S2105, E157, CoA and a water molecule bound to Mg^{2+} (site I). For each simulated reaction step, we computed the PMF by evolving the Hamiltonian of the system with respect to the λ parameter, which was defined as a linear combination of relevant interatomic distances (d) involved in the reaction. For instance, in the step 1a reaction, where the bond between of OγS2105 and HγS2105 is stretched, causing the interatomic distance of OγS2105 with respect to OεE157 to shorten as OγS2105 approaches the PβCoA atom in the nucleophilic attack, the λ parameter was expressed as a collective variable, CV1a, in which we linearly combined the three atomic distances concerning the reaction:

$$CV1a = d(O\gamma S2105 \leftrightarrow H\gamma S2105) - d(H\gamma S2105 \leftrightarrow O\varepsilon E157) - d(O\gamma S2105 \leftrightarrow P\beta CoA)$$

In this way, we obtained a plot of external work W_i done on the system for each trajectory, and the PMF extracted by the Jarzynski estimator, with respect to the collective variable CV1a (**Figure S13)**. At the end of the simulated reaction steps, we collected and included in **Table I** a series of significant interatomic distances observed for the reactant, transition states, intermediates, and product structure. It

is important to emphasize that the transition state structures contained in the table refer to the configurations extracted from the highest point of the PMF profiles.

Step 1a: In this step, the proton transfer from the hydroxyl group of S2105 to OεE157, concerted with the nucleophilic attack to the PβCoA (**Figure 6A,1a)**, was simulated starting from the initial configuration (**Figure 6A, R**) prepared using the aforementioned procedure. For this reaction we changed the collective variable CV1a from -5.5 Å to -0.9 Å, where the starting value corresponds to the linear combination of the interatomic distances in the starting configuration, while the final value is the predicted collective variable at the end of the reaction. A minimum energy point was found along the PMF path which corresponds to CV1a = -1.0 (**Figure S13**). From this point the structure of the IM1a intermediate was extracted. IM1a corresponds to a PptT-CoA/ACP complex with a Mg^{2+} distorted coordination sphere (**Figure 6A**) where the distances between OγS2105-PβCoA and PβCoA-OαCoA are 1.85 Å and 1.83 Å, respectively (**Table I**). The geometry of the complex and the isometric axial distances between the entering and the leaving group suggests that the nucleophilic substitution at phosphorus could take place with a unimolecular SN1 associative mechanism, according to the Mildvan model[43]. In addition, it was observed that the dihedral angle Oγ-Cα-Cβ-N of S2105 changes its value along trajectories from 90˚ to 0˚, while the Pα-Oα-Pβ angle is flipped by ~180˚ from its initial position. We suggest that this rotation might be the reaction "driving force" implied into serine-pyrophosphate distance reduction and into nucleophilic attack.

Step 1b: To simulate the alternative concerted proton transfer – nucleophilic attack pathway, where a metal-bound water molecule, activated by the nearby E157, deprotonates the hydroxyl group of S2105 (**Figure 6A,1b**), we defined the collective variable of the reaction, CV1b, as the linear combination of the following atomic distances:

$$CV1b = d(H_1 \leftrightarrow O_{(H_2O)}) - d(H_1 \leftrightarrow O\varepsilon E157) + d(O\gamma S2105 \leftrightarrow H\gamma S2105)$$

$$-d(H\gamma S2105 \leftrightarrow O_{(H_2O)}) - d(O\gamma S2105 \leftrightarrow P\beta CoA)$$

As for step 1a, we obtained the PMF with respect to the collective variable, which we varied from -7.5 Å to 1.0 Å (**Figure S14**). For this step, we observed the formation of a PptT-CoA/ACP complex, referred to as intermediate IM1b, at the end of the reaction (**Figure 6A**). In step 1b, in contrast to step 1a, we were able to extract the free energy of the reaction by the Jarzynski equality using only 8 work energy profiles among the set of 96 trajectories. The remaining 88 realizations were discarded because they led to a product where, unlike IM1b, the Oγ of S2105 remains protonated due to proton exchange with a metal-bound water molecule (**Figure S15**).

Step 2a: Starting from the intermediate IM1a, formed in the energetically more favorable pathway step 1a, we prepared the initial configurations for step 2a. Therefore, the interatomic distances OγS2105-PβCoA and PβCoA-OαCoA were harmonically restrained around their initial value. To simulate the leaving group dissociation (**Figure 6A,2a**), we elongated the PβCoA-OαCoA bond from 1.83 to 4.0 Å, allowing us to extract the intermediate IM2a structure (**Figure 6A**) from the nearest trajectories to the PMF at the local minimum (**Figure S16**). Out of a total of 96 trajectories, we used 67 work profiles for this step. In the remaining 29 trajectories, the Oα is protonated by a metal-bound water molecule and the energy profile does not fall in a local minimum. Consequently, these trajectories were excluded from further analysis. In the intermediate IM2a, the Oα of the 3',5'-ADP moiety is separated from PβCoA by 3.58 Å (**Table I**).

Step 3: In this step we simulated the protonation of the 3',5'-ADP moiety on Oα by an activated metal-bond water molecule, which in a concerted way abstracts the proton Hγ bonded to Oε of E157 (**Figure 6A,3**). To quantify this process, we introduced a collective variable (CV3), defined as follows:

$$CV3 = d(H_1 \leftrightarrow O_\alpha) - d(H_1 \leftrightarrow O_{(H_2O)}) - d(O\varepsilon E157 \leftrightarrow H\gamma E157) + d(H\gamma E157 \leftrightarrow O_{(H_2O)})$$

The CV3 value varied from -0.8 to 1.1 Å (**Figure S17**). This reaction step is completely spontaneous. Along the reaction path, IM2a requires overcoming an energy barrier of merely 0.2 kcal/mol to proceed, resulting in the formation of P1a (**Figure 6A**).

Step 2b: In this step, we conducted simulations involving the same reactions as described in step 3, but with the added dissociation of the leaving group. This reaction mechanism starts from IM1a, instead of IM2a (**Figure 6A,2b)**, and leads to the formation of the product P1b (**Figure 6A**). As in the previous steps, we defined a collective variable as a linear combination of interatomic distances, which we changed in all SMD replicates:

$$CV2b = d(H_1 \leftrightarrow O_\alpha) - d(H_1 \leftrightarrow O_{((H_2O))}) - d(O\varepsilon E157 \leftrightarrow H\gamma E157) - d(H\gamma E157 \leftrightarrow O_{((H_2O))})$$

$$-d(P\beta CoA \leftrightarrow O_\alpha)$$

The calculated energy barrier for step 2b is 15.6 kcal/mol (**Figure S18**), which is higher than the activation energy of 10.8 kcal/mol (**Figure 6B**) observed for the reaction pathway where step 3 follows step 2a consecutively. Consequently, it can be concluded that the reaction pathway involving step 2b is less energetically favorable.

Extracting the reaction energy profile – The relevant equations enabling the calculation of the free energy profiles are shown below. For a more comprehensive understanding of the theory, we refer to the work by Park and colleagues[20]. In Steered Molecular Dynamics (SMD), an external time-dependent perturbation is applied on the system in such a way its Hamiltonian H (r,λ) evolves from an initial state λ_0 to a final state λ_1, where r indicates a configuration of the whole system, while λ represents a reaction coordinate. If the system evolves through a non-equilibrium process, the potential mean force ΔF and the work W, which represents the external work performed to change the reaction coordinate from λ_0 to λ_1, are related to each other by the Jarzynski identity:

$$e^{(-\beta\Delta F)} = < e^{(-\beta W)} > \qquad (1)$$

where $\beta = \frac{1}{k_B T}$, with k_B and T being the Boltzmann constant and the temperature, respectively. The brackets represent an average taken over an ensemble of trajectories, assuming that the initial ensemble is equilibrated. To perturb the Hamiltonian of the unperturbed system, a harmonic potential with a force constant k is chosen. This potential displaces the reaction coordinate at a constant velocity v, following the equation:

$$H(r,\lambda) = H_0(r) + \frac{1}{2}k[\lambda(r) - \lambda_0 - vt]^2 \qquad (2)$$

Consequently, the free energy of a process along a reaction coordinate can be computed by performing a number of finite time transformations, collecting the work done at each time step, and then properly averaging it as in equation (1).

The free energy ΔF for a reaction, the so called Potential Mean Force (PMF), is then estimated as a function of the λ parameter for a set of N collected works with the following Jarzynski estimator (JE):

$$\Delta F = -\frac{1}{\beta}\ln\left(\frac{1}{N}\sum_{i=1}^{N} e^{-\beta W_i}\right)$$

where W_i is the work performed on the system along the i^{th} trajectory. However, the Jarzynski estimator can suffer from gross inaccuracy, especially when poorly sampled low-work values dominate the calculation, particularly if the standard deviation of the work distribution is greater than $k_B T$[50]. In this work, we have adopted one of the two extrapolation methods proposed by Ytreberg et al.[18], which correct the bias introduced by the Jarzynski estimator. In particular, the cumulative integral (CI) extrapolation improves standard non-equilibrium estimates of the free energy using a small data set of work values. Remarkably, this approach allows us to achieve reliable results with only 5-40 times less data than is theoretically needed to accurately estimate ΔF.

FIGURES

Figure 1 - Biophysical and biochemical characterization of PptT. (**A**) Schematic representation of the post-translational phosphopantetheinylation by a PPTase. The PPTase transfers the phosphopantetheine (PPant) moiety from Coenzyme A (CoA) to a conserved serine residue on the apo-ACP, resulting in the formation of holo-ACP. (**B**) Thermal stability of PptT purified in the absence of divalent cations and following subsequent addition of 1 mM M^{2+}(Ca^{2+}, Mg^{2+}, Mn^{2+}, Co^{2+} and Ni^{2+}) and 50 μM CoA or 3',5'-ADP. The empty histogram bars represent approximate T_m values. (**C**) Activation time-course of the ACP domain (2042-2188) of PpsC by PptT. The transfer of the Ppant group from CoA to the ACP domain is visualized on a 10% native polyacrylamide gel supplemented with 2.5 M urea, either in the

absence of M^{2+} or in the presence of 1 mM $CaCl_2$, $MgCl_2$ or $MnCl_2$ at 15 and 60 min intervals. The control corresponds to the inactivated form of the ACP domain.

Figure 2 - Crystal structures of PptT. Ribbon representations of PptT are shown for (**A**) the apo form and for the complexes with (**B**) CoA and (**C**) 3',5'-ADP. Electron density 2Fo-Fc SA omit maps are contoured at 1s level. (**D**) To highlight differences in the positioning of key residues and cations, a structural superimposition of all three structures is presented. Residue side chains and CoA are depicted in ball-and-stick mode and color-coded according to atom type (blue for nitrogen, red for oxygen, black for phosphate, and orange for sulfur). The Mn^{2+} and Mg^{2+} ions at sites I and II are colored dark purple and light purple, respectively. Water molecules are represented as red spheres. All figures are in the same orientation.

Figure 3 - Crystal structure of the PptT-CoA/ACP complex. (**A**) The surface representation depicts four PPTases (colored in blue, yellow, purple, and green) and two ACPs (shaded in light and dark gray) within the asymmetric unit. CoA molecules are visualized in a ball-and-stick representation, following the color code introduced in Figure 2. (**B**,**C**) Close-up views showing the ACP domain sandwiched between two PptT molecules. Patches of residues involved in polar and non-polar interactions at the PptT-ACP interface identified using the PDBePISA server[44], are colored in brown. Hydrogen bond interactions are depicted as black dashed lines. The position of the mutated S2105A is indicated with a brown sphere. Figures in (**B**) and (**C**) are presented in the same orientation.

Figure 4 - Tunnel entrance for the pantothenic acid group of CoA. Surface representation of residues E157, Y160, W170 and F173 delineating the tunnel entrance of PptT (**A**) in the absence and (**B**) in the presence of CoA. Interactions with the Ppant arm are predominantly of van der Waals nature. Distance values between closest carbon atoms are indicated. CoA and residues are shown as sticks (carbon and phosphate, black; nitrogen, blue; oxygen, red).

Figure 5 - View of the CoA ligand in PptT alone and in complex with the ACP domain, obtained through molecular dynamic simulations. In the absence of ACP, the main conformations of CoA are shown, with Oβ-Pβ-Oα-Pα dihedral angle values of (**A**) 176° and (**B**) -77°. In the Pβ-Oα-Pα bridge, the Oα oxygen atom is alternatively oriented inside and outside the active site. In both cases, the interaction between the Mg^{2+} ion and the Oβ atom is not affected and remains stable, around 1.9 Å. (**C**) In the presence of ACP, the Oβ-Pβ-Oα-Pα dihedral angle is stabilized around a value of 160°, similar to the one observed in (**A**). However, the Pβ phosphate group has rotated and is replaced by a water molecule that coordinates with the Mg^{2+} ion. The ACP residue S2105 establishes stable hydrogen bonds with residue E157 and the β-phosphate group. All figures are presented in the same orientation.

Figure 6 - Schematic representations of the simulated reaction mechanism. (**A**) Starting from the top, a schematic representation and a reduced view of the Reactant's active site, labeled as R, are provided. On the left side, we illustrate the proton transfer concerted to nucleophilic attack, modeled by step 1a, which leads to the formation of IM1a. Following this, in step 2a, we showcase the dissociation of the 3',5'-ADP moiety from the PptT-CoA/ACP complex, leading to the formation of IM2a. Finally, step 3 follows step 2a, during which the 3',5'-ADP moiety abstracts a proton from an activated metal-bound water molecule. On the right side, we present the alternative step 1b pathway, where the proton is abstracted by an activated metal-bound water molecule, leading to the formation of IM1b. Finally, we illustrate the step 2b pathway, where the dissociation of the 3',5'-ADP is catalyzed by the protonation of Oα, resulting in the formation of P1b. (**B**) Energy profile for the phosphopantetheinyl transfer reaction. The energy profile was obtained from cumulative integral extrapolation of external works performed through Steered Molecular Dynamics. Black dashed lines indicate the energy profile of step 1a, while blue dashed lines represent its alternative pathway, step 1b. The energy profile corresponding to step 2a is depicted in green dashed lines, while steps 2b and 3 are indicated by red and dark-red dash lines, respectively. Snapshots of the active site are represented in the same orientation.

TABLES

Table I: Selected distances for the reactant, transition states, intermediates, and product structures in all the simulated steps. All values reported are in Angstroms.

	R	TS1a	TS1b	IM1a	IM1b	TS2a	TS2b	IM2a	TS3	P1a	P1b
OγS2105-HγS2105	0.96	1.48	1.83	1.77	2.90	3.03	3.12	3.91	4.12	4.00	4.11
HγS2105-OεE157	1.81	1.14	3.12	1.05	2.94	1.19	1.31	1.14	1.15	1.57	1.80
OγS2105-PβCoA	4.66	2.74	2.83	1.85	1.78	1.70	1.73	1.68	1.67	1.69	1.68
PβCoA-OαCoA	1.66	1.73	1.69	1.83	1.84	3.03	2.69	3.58	3.81	4.04	3.28
H1 (H_2O)-OαCoA	3.44	3.20	5.28	4.22	5.89	3.52	1.47	1.45	1.39	1.07	1.08

H1 (H_2O)-OεE157	1.99	2.53	1.16	3.45	1.00	4.54	2.94	2.85	2.81	3.13	2.85
HγS2105-O (H_2O)	2.97	2.75	1.09	2.50	0.95	2.12	1.66	1.50	1.32	1.07	1.04

AUTHOR INFORMATION

Corresponding Authors

Marie Brut - LAAS-CNRS, Université de Toulouse, CNRS, UPS, Toulouse, France

https://orcid.org/0000-0002-2218-052X

Email : marie.brut@laas.fr

Lionel Mourey - Institut de Pharmacologie et de Biologie Structurale (IPBS), Université de Toulouse, CNRS, Université Toulouse III - Paul Sabatier (UT3), Toulouse, France

https://orcid.org/0000-0002-8259-1259

Email : lionel.mourey@ipbs.fr

Jean-Denis Pedelacq - Institut de Pharmacologie et de Biologie Structurale (IPBS), Université de Toulouse, CNRS, Université Toulouse III - Paul Sabatier (UT3), Toulouse, France

https://orcid.org/0000-0002-3202-2517

Email : jean-denis.pedelacq@ipbs.fr

Author Contributions

$JDP supervised the study. SG, AF, MCN, CCa, KR, YR, SS, and JDP conducted and analyzed the biochemistry and structural biophysics experiments. SF, GC, and MB performed the molecular modeling coupled with QM/MM calculations. JDP wrote the paper with contributions from all the authors. CCh, CG, LM, and JDP provided funding.

Funding sources

This work was supported by the Agence Nationale de la Recherche (XPKS-MYCO, grant 09-BLAN-0298-01; PPTases, grant ANR-16-CE18-0011-01) and the Région Midi-Pyrénées (MYCA, grants 34249 and 09005193; TUBCAN, grant 11052698).

ACKNOWLDEGMENT

The equipment used for differential scanning fluorimetry, crystallization experiments and X-ray crystallography are part of the Integrated Screening Platform of Toulouse (PICT, IBiSA). We thank Tom Terwilliger for careful advice concerning the structure determination of the PptT-ACP structure. We thank the scientific staff of the European Synchrotron Radiation Facility (Grenoble, France), SOLEIL (Gif sur Yvette, France) and ALBA (Barcelona, Spain). We particularly thank the staff of beamline ID23-2 and ID29 at the European Synchrotron Radiation Facility, beamline XALOC at ALBA, and PROXIMA-1 at SOLEIL, where the crystallographic experiments were conducted. We finally thank the CALMIP mesocenter, where the simulations were performed using HPC resources (Grants P1237 and P22015).

REFERENCES

(1) Weissman, K. J.; Leadlay, P. F. Combinatorial Biosynthesis of Reduced Polyketides. *Nat. Rev. Microbiol.* **2005**, *3* (December), 925–936. https://doi.org/10.1038/nrmicro1287.

(2) Flugel, R. S. Holo-(Acyl Carrier Protein) Synthase and Phosphopantetheinyl Transfer in Escherichia Coli. *J. Biol. Chem.* **2000**, *275* (2), 959–968. https://doi.org/10.1074/jbc.275.2.959.

(3) Leblanc, C.; Prudhomme, T.; Tabouret, G.; Ray, A.; Burbaud, S.; Cabantous, S.; Mourey, L.; Guilhot, C.; Chalut, C. 4′-Phosphopantetheinyl Transferase PptT, a New Drug Target Required for Mycobacterium Tuberculosis Growth and Persistence In Vivo. *PLoS Pathog.* **2012**, *8* (12). https://doi.org/10.1371/journal.ppat.1003097.

(4) Ottavi, S.; Scarry, S. M.; Mosior, J.; Ling, Y.; Roberts, J.; Singh, A.; Zhang, D.; Goullieux, L.; Roubert, C.; Bacqué, E.; Lagiakos, H. R.; Vendome, J.; Moraca, F.; Li, K.; Perkowski, A. J.; Ramesh, R.; Bowler, M. M.; Tracy, W.; Feher, V. A.; Sacchettini, J. C.; Gold, B. S.; Nathan, C. F.; Aubé, J. In Vitro and in Vivo Inhibition of the Mycobacterium Tuberculosis Phosphopantetheinyl Transferase PptT by Amidinoureas. *J. Med. Chem.* **2022**, *65* (3), 1996–2022. https://doi.org/10.1021/acs.jmedchem.1c01565.

(5) Ballinger, E.; Mosior, J.; Hartman, T.; Burns-huang, K.; Gold, B.; Morris, R.; Goullieux, L.; Blanc, I.; Vaubourgeix, J.; Lagrange, S.; Fraisse, L.; Sans, S.; Couturier, C.; Bacqué, E.; Rhee, K.; Scarry, S. M.; Aubé, J.; Yang, G.; Ouerfelli, O.; Schnappinger, D.; Ioerger, T. R.; Engelhart, C. A.; Mcconnell, J. A.; Mcaulay, K.; Fay, A.; Roubert, C.; Sacchettini, J.; Nathan, C. Opposing Reactions in Coenzyme A Metabolism Sensitize Mycobacterium Tuberculosis to Enzyme Inhibition. *Science* **2019**, *363*, 1–8. https://doi.org/10.1126/science.aau8959.

(6) Rottier, K.; Faille, A.; Prudhomme, T.; Leblanc, C.; Chalut, C.; Cabantous, S.; Guilhot, C.; Mourey, L.; Pedelacq, J.-D. J. D. Detection of Soluble Co-Factor Dependent Protein Expression in Vivo: Application to the 4'-Phosphopantetheinyl Transferase PptT from Mycobacterium Tuberculosis. *J. Struct. Biol.* **2013**, *183* (3), 320–328. https://doi.org/10.1016/j.jsb.2013.07.010.

(7) Mofid, M. R. R.; Finking, R.; Essen, L. O. O.; Marahiel, M. a a. Structure-Based Mutational Analysis of the 4 '-Phosphopantetheinyl Transferases Sfp from Bacillus Subtilis: Carrier

Protein Recognition and Reaction Mechanism. *Biochemistry* **2004**, *43* (14), 4128–4136. https://doi.org/10.1021/Bi036013h.

(8) Parris, K. D.; Lin, L.; Tam, A.; Mathew, R.; Hixon, J.; Stahl, M.; Fritz, C. C.; Seehra, J.; Somers, W. S. Crystal Structures of Substrate Binding to Bacillus Subtilis Holo-(Acyl Carrier Protein) Synthase Reveal a Novel Trimeric Arrangement of Molecules Resulting in Three Active Sites. *Structure* **2000**, *8* (8), 883–895. https://doi.org/10.1016/S0969-2126(00)00178-7.

(9) Nguyen, M. C.; Saurel, O.; Carivenc, C.; Gavalda, S.; Saitta, S.; Tran, M. P.; Milon, A.; Chalut, C.; Guilhot, C.; Mourey, L.; Pedelacq, J. D. Conformational Flexibility of Coenzyme A and Its Impact on the Post-Translational Modification of Acyl Carrier Proteins by 4′-Phosphopantetheinyl Transferases. *FEBS J.* **2020**, 1–18. https://doi.org/10.1111/febs.15273.

(10) Beld, J.; Sonnenschein, E. C.; Vickery, C. R.; Noel, J. P.; Burkart, M. D. The Phosphopantetheinyl Transferases: Catalysis of a Post-Translational Modification Crucial for Life. *Nat. Prod. Rep.* **2014**, *31* (1), 61–108. https://doi.org/10.1039/c3np70054b.

(11) Faille, A.; Gavalda, S.; Slama, N.; Lherbet, C.; Maveyraud, L.; Guillet, V.; Laval, F.; Quémard, A.; Mourey, L.; Pedelacq, J. J.-D. Insights into Substrate Modification by Dehydratases from Type I Polyketide Synthases. *J. Mol. Biol.* **2017**, *429* (10), 1554–1569. https://doi.org/10.1016/j.jmb.2017.03.026.

(12) Pedelacq, J. D.; Nguyen, H. B.; Cabantous, S.; Mark, B. L.; Listwan, P.; Bell, C.; Friedland, N.; Lockard, M.; Faille, A.; Mourey, L.; Terwilliger, T. C.; Waldo, G. S. Experimental Mapping of Soluble Protein Domains Using a Hierarchical Approach. *Nucleic Acids Res.* **2011**, *39* (18), e125. https://doi.org/10.1093/nar/gkr548.

(13) Bunkoczi, G.; Pasta, S.; Joshi, A.; Wu, X.; Kavanagh, K. L.; Smith, S.; Oppermann, U. Mechanism and Substrate Recognition of Human Holo ACP Synthase. *Chem. Biol.* **2007**, *14* (November), 1243–1253. https://doi.org/10.1016/j.chembiol.2007.10.013.

(14) Chirgadze, N. Y.; Briggs, S. L.; McAllister, K. A.; Fischl, A. S.; Zhao, G. Crystal Structure of Streptococcus Pneumoniae Acyl Carrier Protein Synthase: An Essential Enzyme in Bacterial Fatty Acid Biosynthesis. *EMBO J.* **2000**, *19* (20), 5281–5287. https://doi.org/10.1093/emboj/19.20.5281.

(15) Vickery, C. R.; Kosa, N. M.; Casavant, E. P.; Duan, S.; Noel, J. P.; Burkart, M. D. Structure, Biochemistry, and Inhibition of Essential 4'-Phosphopantetheinyl Transferases from Two Species of Mycobacteria. *ACS Chem. Biol.* **2014**, *9* (9), 1939–1944. https://doi.org/10.1021/cb500263p.

(16) Tufar, P.; Rahighi, S.; Kraas, F. I.; Kirchner, D. K.; Löhr, F.; Henrich, E.; Köpke, J.; Dikic, I.; Güntert, P.; Marahiel, M. A.; Dötsch, V. Crystal Structure of a PCP/Sfp Complex Reveals the Structural Basis for Carrier Protein Posttranslational Modification. *Chem. Biol.* **2014**, *21* (4), 552–562. https://doi.org/10.1016/j.chembiol.2014.02.014.

(17) Stewart, J. J. P. Optimization of Parameters for Semiempirical Methods V: Modification of NDDO Approximations and Application to 70 Elements. *J. Mol. Model.* **2007**, *13* (12), 1173–1213. https://doi.org/10.1007/s00894-007-0233-4.

(18) Ytreberg, F. M.; Zuckerman, D. M. Efficient Use of Nonequilibrium Measurement to Estimate Free Energy Differences for Molecular Systems. *J. Comput. Chem.* **2004**, *25* (14), 1749–1759. https://doi.org/10.1002/jcc.20103.

(19) Boubeta, F. M.; Contestín García, R. M.; Lorenzo, E. N.; Boechi, L.; Estrin, D.; Sued, M.; Arrar, M. Lessons Learned about Steered Molecular Dynamics Simulations and Free Energy Calculations. *Chem. Biol. Drug Des.* **2019**, *93* (6), 1129–1138. https://doi.org/10.1111/cbdd.13485.

(20) Park, S.; Schulten, K. Calculating Potentials of Mean Force from Steered Molecular Dynamics

Simulations. *J. Chem. Phys.* **2004**, *120* (13), 5946–5961. https://doi.org/10.1063/1.1651473.

(21) Jarzynski, C. A Nonequilibrium Equality for Free Energy Differences. *Phys. Rev. Lett.* **1997**, *78* (14), 2690–2693. https://doi.org/10.1103/PhysRevLett.78.2690.

(22) Brut, M.; Estève, A.; Landa, G.; Renvez, G.; Djafari Rouhani, M. The Static Modes: An Alternative Approach for the Treatment of Macro- and Bio-Molecular Induced-Fit Flexibility. *Eur. Phys. J. E* **2009**, *28* (1), 17–25. https://doi.org/10.1140/epje/i2008-10397-0.

(23) Whicher, J. R.; Smaga, S. S.; Hansen, D. A.; Brown, W. C.; Gerwick, W. H.; Sherman, D. H.; Smith, J. L. Cyanobacterial Polyketide Synthase Docking Domains%: A Tool for Engineering Natural Product Biosynthesis. *Chem. Biol.* **2013**, *20* (11), 1340–1351. https://doi.org/10.1016/j.chembiol.2013.09.015.

(24) Carivenc, C.; Maveyraud, L.; Blanger, C.; Ballereau, S.; Roy-Camille, C.; Nguyen, M. C.; Génisson, Y.; Guilhot, C.; Chalut, C.; Pedelacq, J. D.; Mourey, L. Phosphopantetheinyl Transferase Binding and Inhibition by Amidino-Urea and Hydroxypyrimidinethione Compounds. *Sci. Rep.* **2021**, *11* (1), 1–10. https://doi.org/10.1038/s41598-021-97197-4.

(25) Singh, A.; Ottavi, S.; Krieger, I.; Planck, K.; Perkowski, A.; Kaneko, T.; Davis, A. M.; Suh, C.; Zhang, D.; Goullieux, L.; Alex, A.; Roubert, C.; Gardner, M.; Preston, M.; Smith, D. M.; Ling, Y.; Roberts, J.; Cautain, B.; Upton, A.; Cooper, C. B.; Serbina, N.; Tanvir, Z.; Mosior, J.; Ouerfelli, O.; Yang, G.; Gold, B. S.; Rhee, K. Y.; Sacchettini, J. C.; Fotouhi, N.; Aubé, J.; Nathan, C. Redirecting Raltitrexed from Cancer Cell Thymidylate Synthase to Mycobacterium Tuberculosis Phosphopantetheinyl Transferase . *Sci. Adv.* **2024**, *10* (11), 1–17. https://doi.org/10.1126/sciadv.adj6406.

(26) Chalut, C.; Botella, L.; de Sousa-D'Auria, C.; Houssin, C.; Guilhot, C. The Nonredundant Roles of Two 4′-Phosphopantetheinyl Transferases in Vital Processes of Mycobacteria. *Proc. Natl. Acad. Sci. U. S. A.* **2006**, *103* (22), 8511–8516. https://doi.org/10.1073/pnas.0511129103.

(27) Luft, J. R.; DeTitta, G. T. A Method to Produce Microseed Stock for Use in the Crystallization of Biological Macromolecules. *Acta Crystallogr. Sect. D Biol. Crystallogr.* **1999**, *55* (5), 988–993. https://doi.org/10.1107/S0907444999002085.

(28) Bergfors, T. Seeds to Crystals. *J. Struct. Biol.* **2003**, *142* (1), 66–76. https://doi.org/10.1016/S1047-8477(03)00039-X.

(29) McCoy, A. J.; Grosse-Kunstleve, R. W.; Adams, P. D.; Winn, M. D.; Storoni, L. C.; Read, R. J. Phaser Crystallographic Software. *J. Appl. Crystallogr.* **2007**, *40* (Pt 4), 658–674. https://doi.org/10.1107/S0021889807021206.

(30) Emsley, P.; Lohkamp, B.; Scott, W. G.; Cowtan, K. Features and Development of Coot. *Acta Crystallogr. D. Biol. Crystallogr.* **2010**, *66* (Pt 4), 486–501. https://doi.org/10.1107/S0907444910007493.

(31) Adams, P. D.; Afonine, P. V; Bunkóczi, G.; Chen, V. B.; Davis, I. W.; Echols, N.; Headd, J. J.; Hung, L.-W.; Kapral, G. J.; Grosse-Kunstleve, R. W.; McCoy, A. J.; Moriarty, N. W.; Oeffner, R.; Read, R. J.; Richardson, D. C.; Richardson, J. S.; Terwilliger, T. C.; Zwart, P. H. PHENIX: A Comprehensive Python-Based System for Macromolecular Structure Solution. *Acta Crystallogr. D. Biol. Crystallogr.* **2010**, *66* (Pt 2), 213–221. https://doi.org/10.1107/S0907444909052925.

(32) Case, D. A.; Cerutti, D. S.; Cheatham, T. E. I.; Darden, T. A.; Duke, R. E.; Giese, T. J.; Gohlke, H.; Goetz, A. W.; Greene, D.; Homeyer, N.; Izadi, S.; Kovalenko, A.; Lee, T. S.; LeGrand, S.; Li, P.; Lin, C.; Liu, J.; Luchko, T.; Luo, R.; Mermelstein, D.; Merz, K. M.; Monard, G.; Nguyen, H.; Omelyan, I.; Onufriev, A.; Pan, F.; Qi, R.; Roe, D. R.; Roitberg, A.; Sagui, C.; Simmerling, C. L.; Botello-Smith, W. M.; Swails, J.; Walker, R. C.; Wang, J.; Wolf, R. M.; Wu, X.; Xiao, L.; York, D. M.; Kollman, P. A. Amber 2017 Reference Man. *Univ.*

California, San Fr. **2017**, AMBER 2017, University of California, San Francisc.

(33) Maier, J. A.; Martinez, C.; Kasavajhala, K.; Wickstrom, L.; Hauser, K. E.; Simmerling, C. Ff14SB: Improving the Accuracy of Protein Side Chain and Backbone Parameters from Ff99SB. *J. Chem. Theory Comput.* **2015**, *11* (8), 3696–3713. https://doi.org/10.1021/acs.jctc.5b00255.

(34) Meagher, K. L.; Redman, L. T.; Carlson, H. A. Development of Polyphosphate Parameters for Use with the AMBER Force Field. *J. Comput. Chem.* **2003**, *24* (9), 1016–1025. https://doi.org/10.1002/jcc.10262.

(35) Allnér, O.; Nilsson, L.; Villa, A. Magnesium Ion-Water Coordination and Exchange in Biomolecular Simulations. *J. Chem. Theory Comput.* **2012**, *8* (4), 1493–1502. https://doi.org/10.1021/ct3000734.

(36) Wang, J.; Wang, W.; Kollman, P. A.; Case, D. A. Automatic Atom Type and Bond Type Perception in Molecular Mechanical Calculations. *J. Mol. Graph. Model.* **2006**, *25* (2), 247–260. https://doi.org/10.1016/j.jmgm.2005.12.005.

(37) Anandakrishnan, R.; Aguilar, B.; Onufriev, A. V. H++ 3.0: Automating PK Prediction and the Preparation of Biomolecular Structures for Atomistic Molecular Modeling and Simulations. *Nucleic Acids Res.* **2012**, *40* (W1), 537–541. https://doi.org/10.1093/nar/gks375.

(38) Price, D. J.; Brooks, C. L. A Modified TIP3P Water Potential for Simulation with Ewald Summation. *J. Chem. Phys.* **2004**, *121* (20), 10096–10103. https://doi.org/10.1063/1.1808117.

(39) Roe, D. R.; Cheatham, T. E. PTRAJ and CPPTRAJ: Software for Processing and Analysis of Molecular Dynamics Trajectory Data. *J. Chem. Theory Comput.* **2013**, *9* (7), 3084–3095. https://doi.org/10.1021/ct400341p.

(40) Humphrey, W.; Dalke, A.; Schulten, K. VMD: Visual Molecular Dynamics. *J. Mol. Graph.* **1996**, *14* (October 1995), 33–38.

(41) Lee, C.; YANG, W.; PARR, R. G. Development of the Colle-Salvetti Correlation-Energy Formula into a Functional of the Electron Density. *Phys. Rev. B, Condens. matter.* **1988**, *37* (2), 785–789. https://doi.org/10.1103/PhysRevB.37.785.

(42) Becke, A. D. Density-Functional Thermochemistry. III: The Role of Exact Exchange. *J. Chem. Phys.* **1993**, *98* (7), 5648–5652. https://doi.org/10.1063/1.464913.

(43) Grimme, S.; Antony, J.; Ehrlich, S.; Krieg, H. A Consistent and Accurate Ab Initio Parametrization of Density Functional Dispersion Correction (DFT-D) for the 94 Elements H-Pu. *J. Chem. Phys.* **2010**, *132*. https://doi.org/10.1063/1.3382344.

(44) Weigend, F.; Ahlrichs, R. Balanced Basis Sets of Split Valence, Triple Zeta Valence and Quadruple Zeta Valence Quality for H to Rn: Design and Assessment of Accuracy. *Phys. Chem. Chem. Phys.* **2005**, *7* (18), 3297–3305. https://doi.org/10.1039/b508541a.

(45) Dunning, T. H. J. Gaussian Basis Sets for Use in Correlated Molecular Calculations. I. The Atoms Boron through Neon and Hydrogen. *J. Chem. Phys.* **1989**, *90*, 1007–1023. https://doi.org/10.1063/1.456153.

(46) Marenich, A. V.; Cramer, C. J.; Truhlar, D. G. Universal Solvation Model Based on Solute Electron Density and on a Continuum Model of the Solvent Defined by the Bulk Dielectric Constant and Atomic Surface Tensions. *J. Phys. Chem. B* **2009**, *113* (18), 6378–6396. https://doi.org/10.1021/jp810292n.

(47) Allen, M.; Tildesley, D. *Computer Simulation of Liquid Al2O3*; Clarendon Press Oxford, 1991; Vol. 18. https://doi.org/10.1088/0953-8984/18/41/001.

(48) Berendsen, H. J. C.; Postma, J. P. M.; Van Gunsteren, W. F.; Dinola, A.; Haak, J. R. Molecular Dynamics with Coupling to an External Bath. *J. Chem. Phys.* **1984**, *81* (8), 3684–3690. https://doi.org/10.1063/1.448118.

(49) Ramírez, C. L.; Zeida, A.; Jara, G. E.; Roitberg, A. E.; Martí, M. A. Improving Efficiency in SMD Simulations through a Hybrid Differential Relaxation Algorithm. *J. Chem. Theory Comput.* **2014**, *10* (10), 4609–4617. https://doi.org/10.1021/ct500672d.

(50) Jarzynski, C. Rare Events and the Convergence of Exponentially Averaged Work Values. *Phys. Rev. E - Stat. Nonlinear, Soft Matter Phys.* **2006**, *73* (4), 1–15. https://doi.org/10.1103/PhysRevE.73.046105.

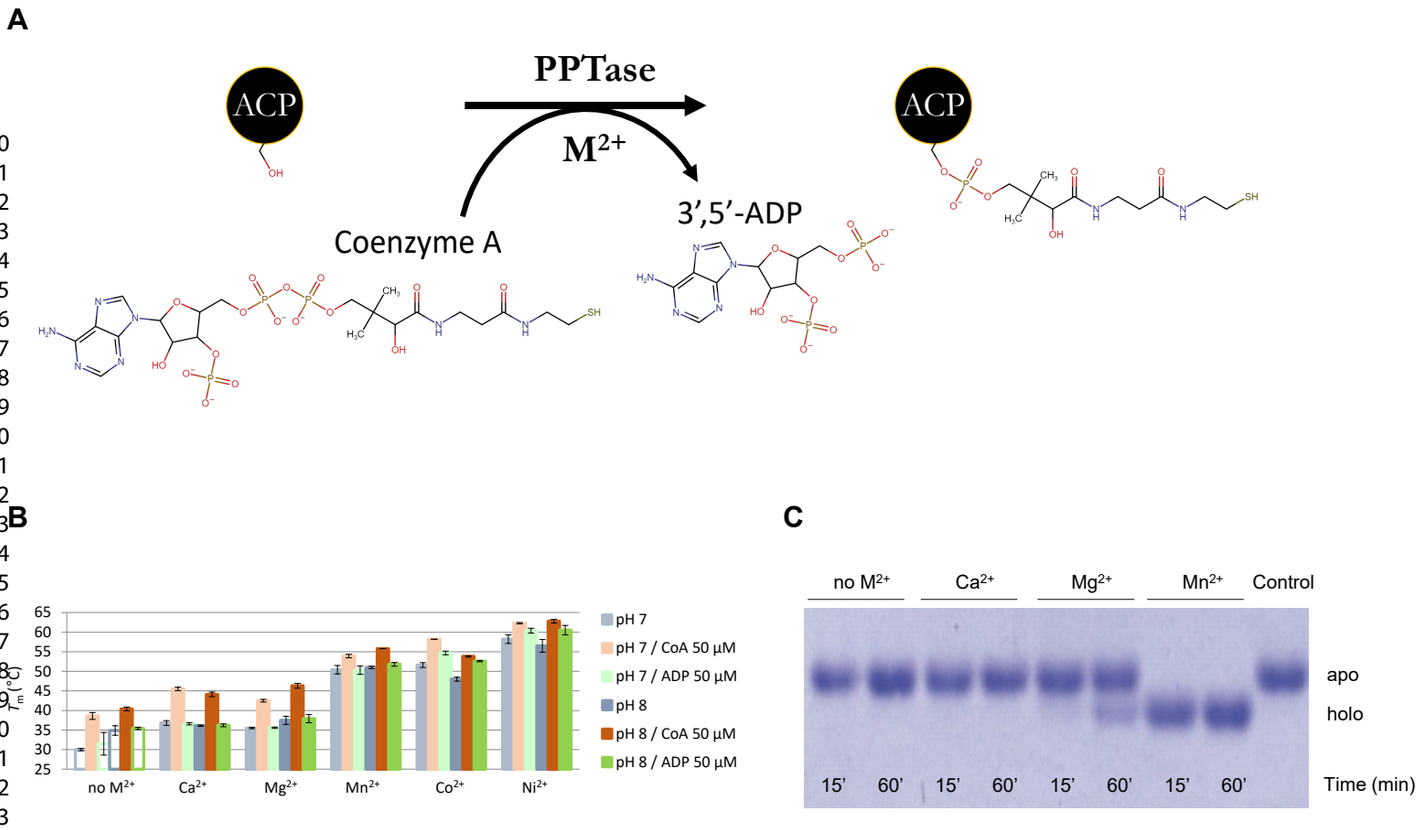

Figure 1 - Biophysical and biochemical characterization of PptT. (**A**) Schematic representation of the post-translational phosphopantetheinylation by a PPTase. The PPTase transfers the phosphopantetheine (PPant) moiety from Coenzyme A (CoA) to a conserved serine residue on the apo-ACP, resulting in the formation of holo-ACP. (**B**) Thermal stability of PptT purified in the absence of divalent cations and following subsequent addition of 1 mM M^{2+}(Ca^{2+}, Mg^{2+}, Mn^{2+}, Co^{2+} and Ni^{2+}) and 50 µM CoA or 3',5'-ADP. The empty histogram bars represent approximate T_m values. (**C**) Activation time-course of the ACP domain (2042-2188) of PpsC by PptT. The transfer of the Ppant group from CoA to the ACP domain is visualized on a 10% native polyacrylamide gel supplemented with 2.5 M urea, either in the absence of M^{2+} or in the presence of 1 mM $CaCl_2$, $MgCl_2$ or $MnCl_2$ at 15 and 60 min intervals. The control corresponds to the inactivated form of the ACP domain.

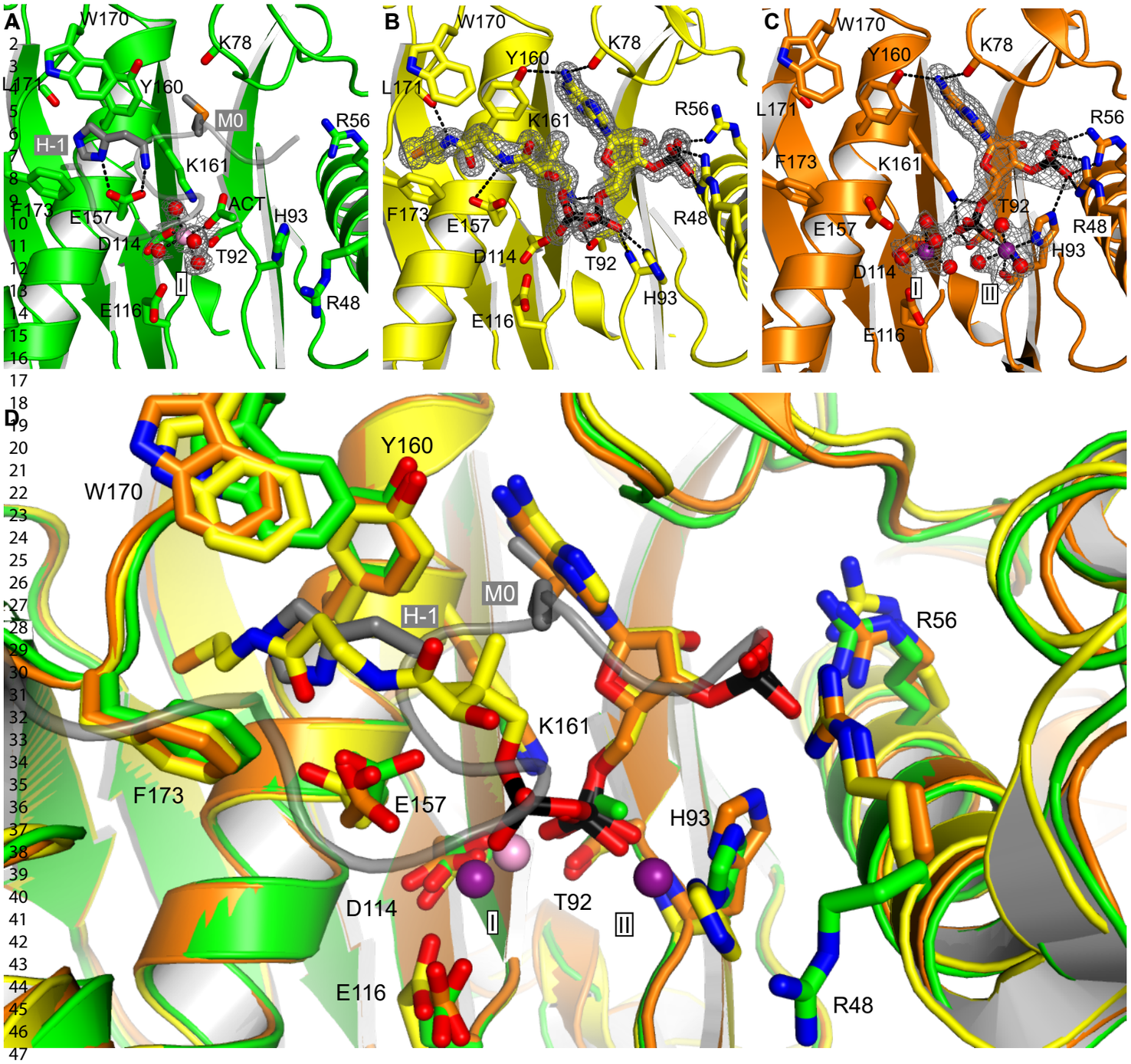

Figure 2 - Crystal structures of PptT. Ribbon representations of PptT are shown for (**A**) the apo form and for the complexes with (**B**) CoA and (**C**) 3',5'-ADP. Electron density 2Fo-Fc SA omit maps are contoured at 1σ level. (**D**) To highlight differences in the positioning of key residues and cations, a structural superimposition of all three structures is presented. Residue side chains and CoA are depicted in ball-and-stick mode and color-coded according to atom type (blue for nitrogen, red for oxygen, black for phosphate, and orange for sulfur). The Mn^{2+} and Mg^{2+} ions at sites I and II are colored dark purple and light purple, respectively. Water molecules are represented as red spheres. All figures are in the same orientation.

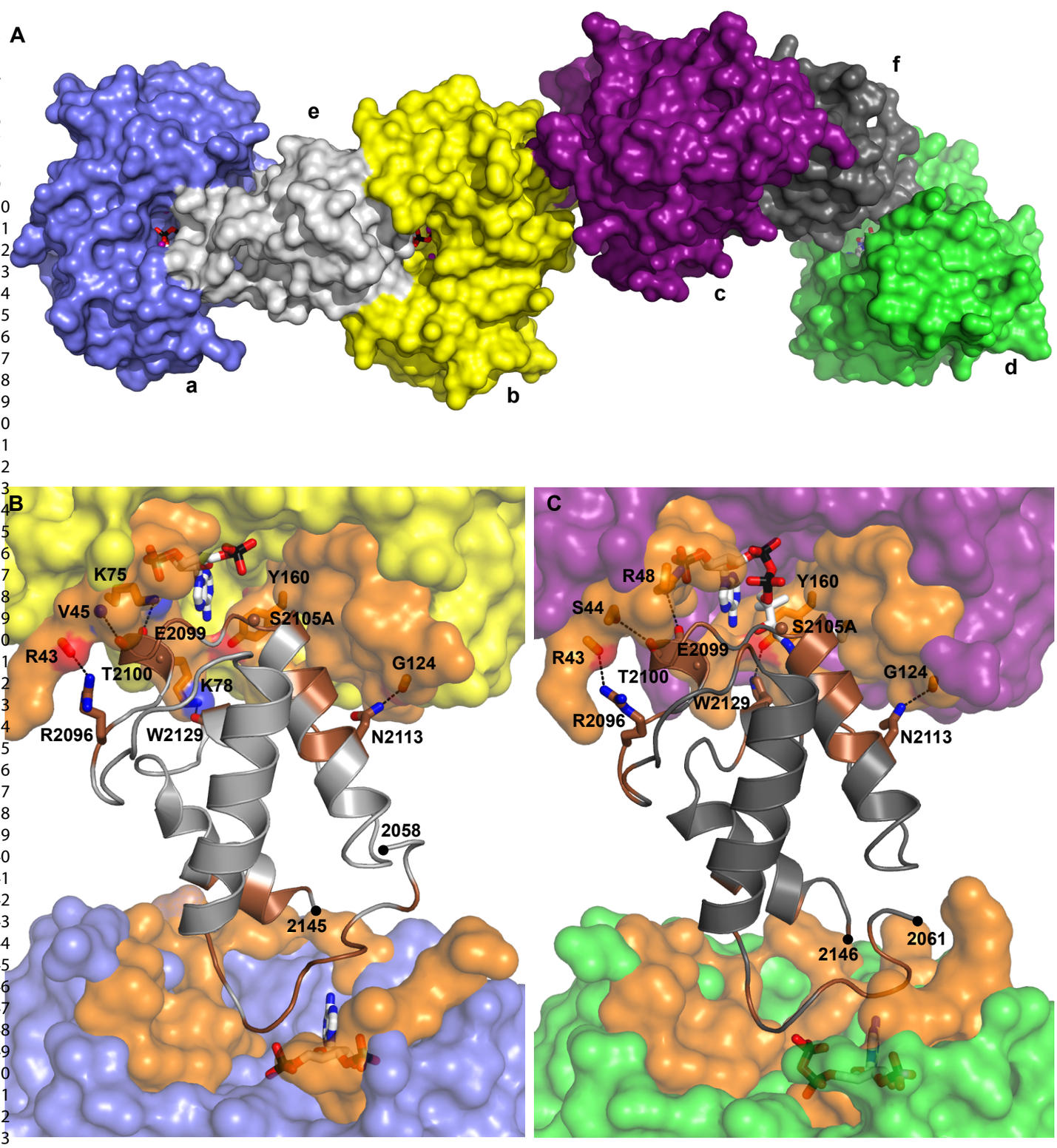

Figure 3 - Crystal structure of the PptT-CoA/ACP complex. (**A**) The surface representation depicts four PPTases (colored in blue, yellow, purple, and green) and two ACPs (shaded in light and dark gray) within the asymmetric unit. CoA molecules are visualized in a ball-and-stick representation, following the color code introduced in Figure 2. (**B**,**C**) Close-up views showing the ACP domain sandwiched between two PptT molecules. Patches of residues involved in polar and non-polar interactions at the PptT-ACP interface identified using the PDBePISA server[44], are colored in brown. Hydrogen bond interactions are depicted as black dashed lines. The position of the mutated S2105A is indicated with a brown sphere. Figures in (**B**) and (**C**) are presented in the same orientation.

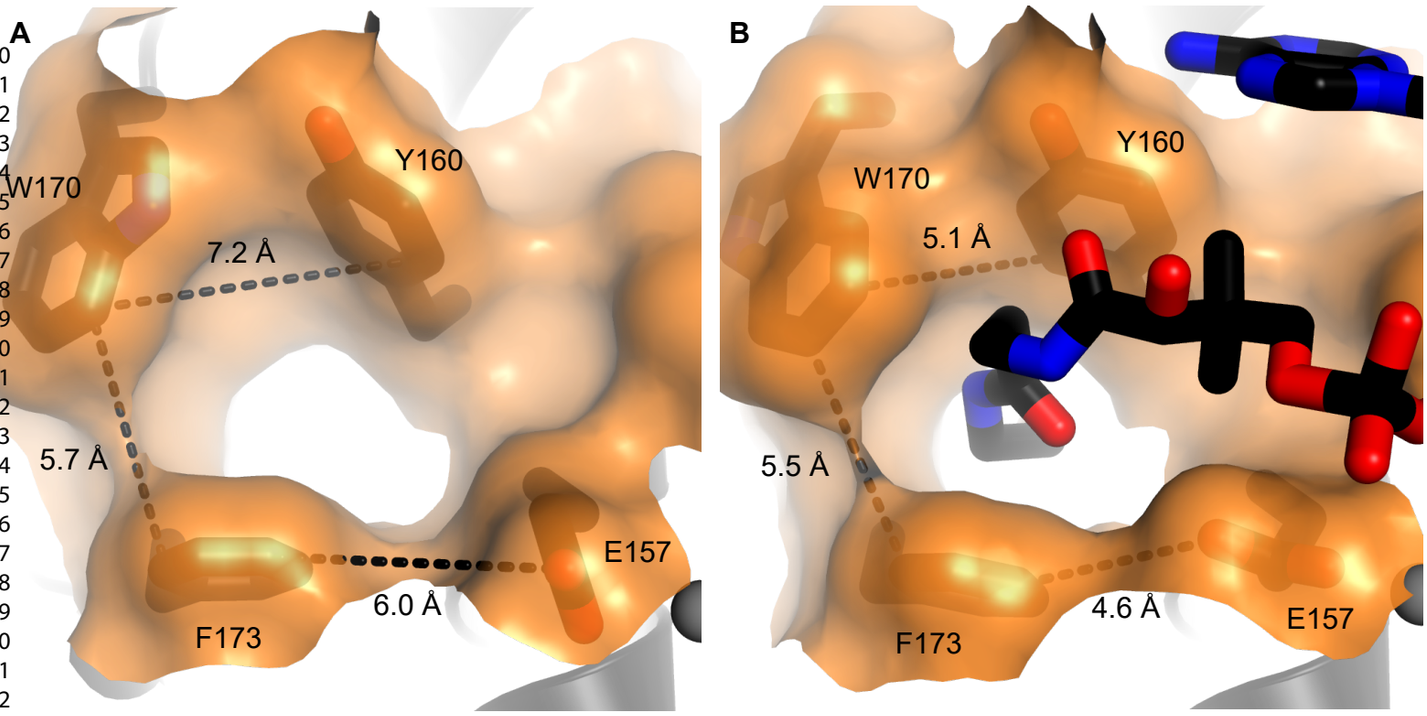

Figure 4 - Tunnel entrance for the pantothenic acid group of CoA. Surface representation of residues E157, Y160, W170 and F173 delineating the tunnel entrance of PptT (**A**) in the absence and (**B**) in the presence of CoA. Interactions with the Ppant arm are predominantly of van der Waals nature. Distance values between closest carbon atoms are indicated. CoA and residues are shown as sticks (carbon and phosphate, black; nitrogen, blue; oxygen, red).

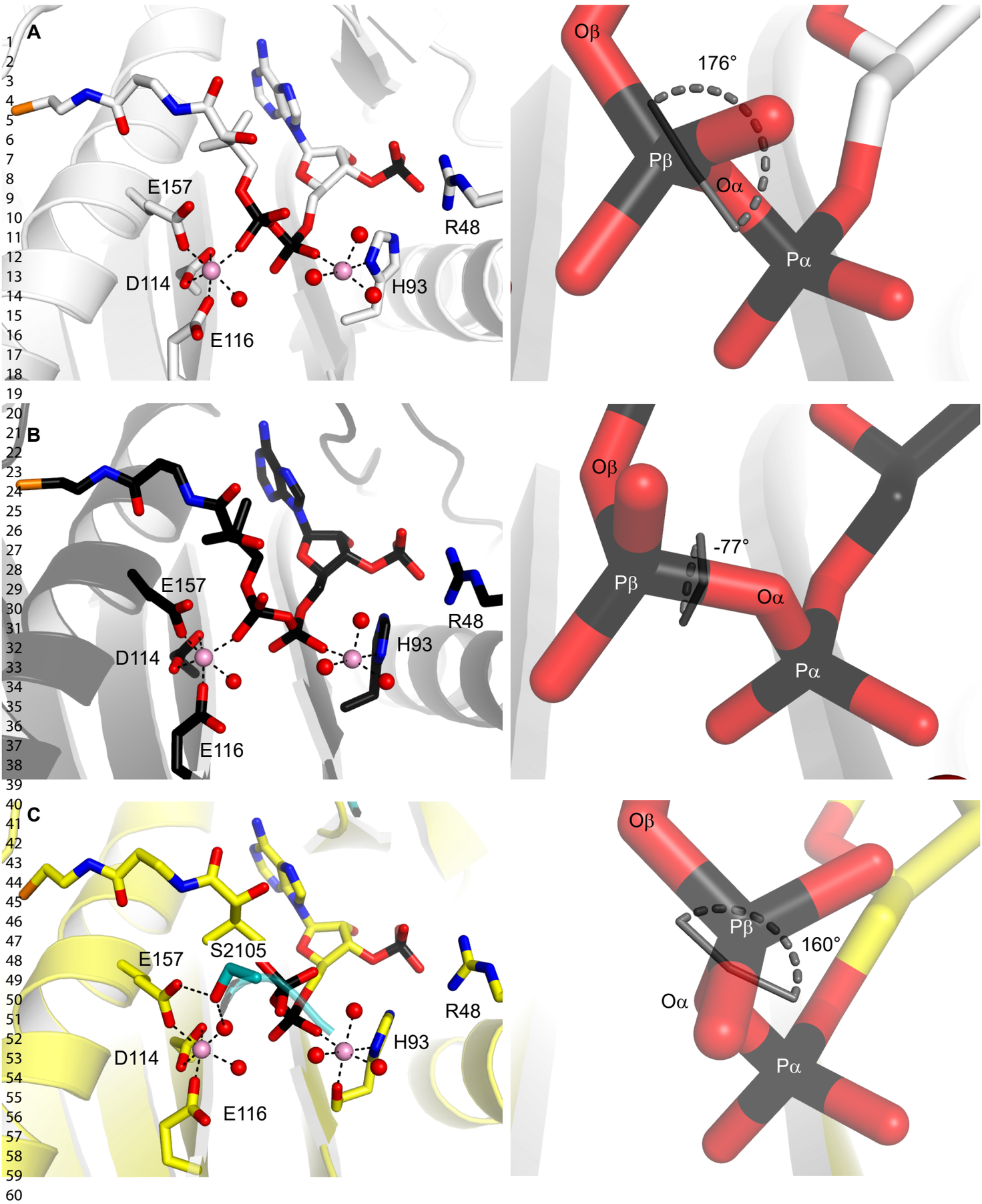

Figure 5 - View of the CoA ligand in PptT alone and in complex with the ACP domain, obtained through molecular dynamic simulations. In the absence of ACP, the main conformations of CoA are shown, with Oβ-Pβ-Oα-Pα dihedral angle values of (**A**) 176° and (**B**) -77°. In the Pβ-Oα-Pα bridge, the Oα oxygen atom is alternatively oriented inside and outside the active site. In both cases, the interaction between the Mg^{2+} ion and the Oβ atom is not affected and remains stable, around 1.9 Å. (**C**) In the presence of ACP, the Oβ -Pβ-Oα-Pα dihedral angle is stabilized around a value of 160°, similar to the one observed in (**A**). However, the Pβ phosphate group has rotated and is replaced by a water molecule that coordinates with the Mg^{2+} ion. The ACP residue S2105 establishes stable hydrogen bonds with residue E157 and the β-phosphate group. All figures are presented in the same orientation.

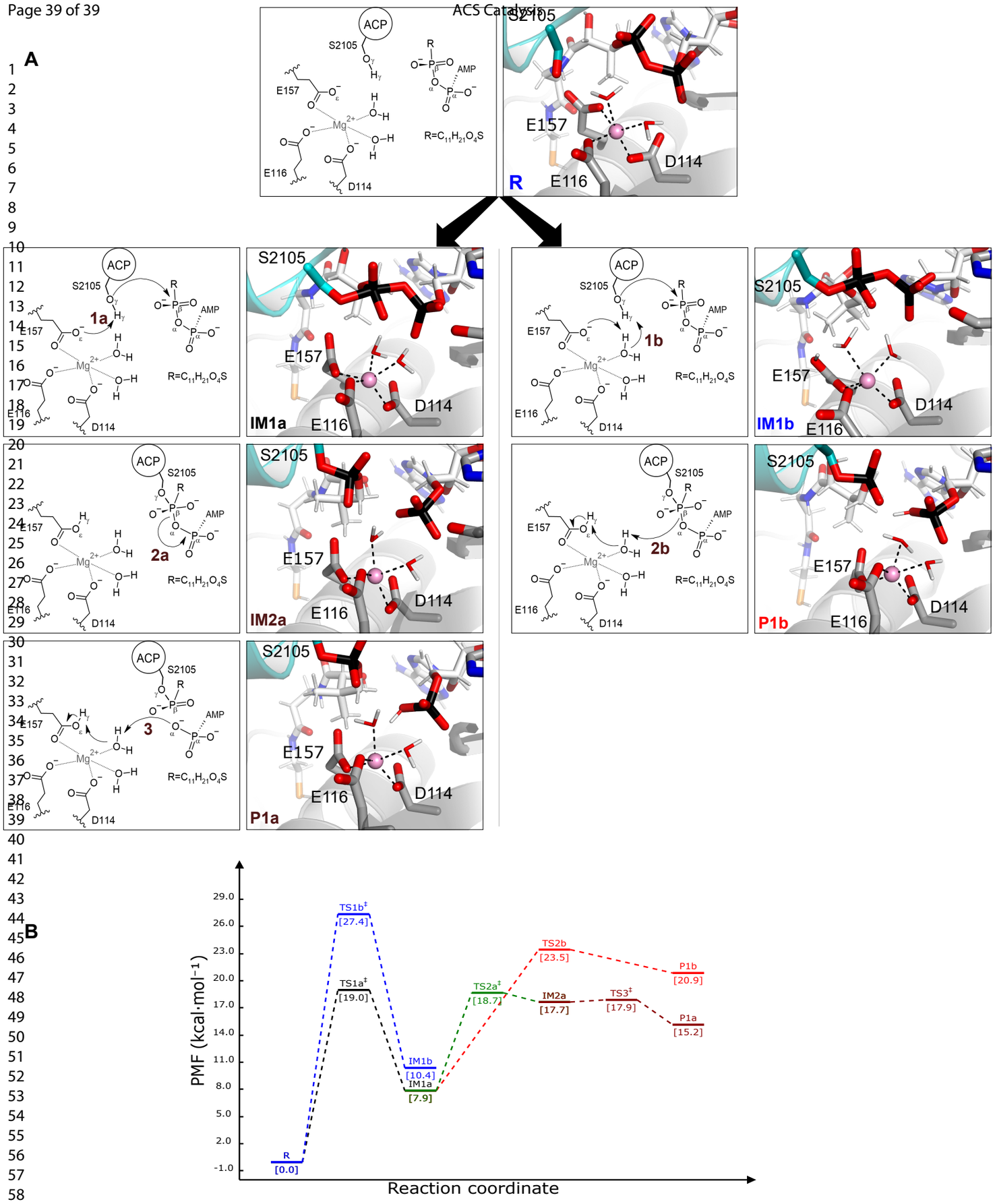

Figure 6 - Schematic representations of the simulated reaction mechanism. (**A**) Starting from the top, a schematic representation and a reduced view of the Reactant's active site, labeled as R, are provided. On the left side, we illustrate the proton transfer concerted to nucleophilic attack, modeled by step 1a, which leads to the formation of IM1a. Following this, in step 2a, we showcase the dissociation of the 3',5'-ADP moiety from the PptT-CoA/ACP complex, leading to the formation of IM2a. Finally, step 3 follows step 2a, during which the 3',5'-ADP moiety abstracts a proton from an activated metal -bound water molecule. On the right side, we present the alternative step 1b pathway, where the proton is abstracted by an activated metal-bound water molecule, leading to the formation of IM1b. Finally, we illustrate the step 2b pathway, where the dissociation of the 3',5'-ADP is catalyzed by the protonation of Oα, resulting in the formation of P1b. (**B**) Energy profile for the phosphopantetheinyl transfer reaction. The energy profile was obtained from cumulative integral extrapolation of external works performed through Steered Molecular Dynamics. Black dashed lines indicate the energy profile of step 1a, while blue dashed lines represent its alternative pathway, step 1b. The energy profile corresponding to step 2a is depicted in green dashed lines, while steps 2b and 3 are indicated by red and dark-red dash lines, respectively. Snapshots of the active site are represented in the same orientation.